PHOTOELECTROCHEMISTRY OF TIO_2 AND THE OXIDATION OF NO_X

A Thesis

by

JONATHAN JAMES FILIP

Submitted to the Graduate and Professional School of
Texas A&M University
in partial fulfillment of the requirements for the degree of

MASTER OF SCIENCE

Chair of Committee,	Dan Zollinger
Co-Chair of Committee,	Qi Ying
Committee Members,	Ying Li
Head of Department,	Zachary Grasley

May 2023

Major Subject: Civil Engineering

ABSTRACT

In this study TiO_2 is used as a photocatalyst for the removal of pollutants via oxidation. The pollutants of interest are nitrogen oxides; the specific gas of use in this study is NO blended with air. This study is an attempt to establish required concentrations of TiO_2 to achieve specific oxidation percentages of NO_x given a constant flowrate, input NO concentration, humidity, and quantum flux input. A comparison of a pure air atmosphere and a nitrogen atmosphere in the testing chamber are included to provide insight to the role O_2 plays in this electrical phenomenon called photocatalysis. A method for producing TiO_2 nanoparticles by using Ti electrodes and a resulting thermal plasma is investigated and tested.

DEDICATION

I would first like to thank my mom for always believing in me and helping me through the hardest times. I would also like to thank Dr. Zollinger for believing in me and putting up with me and always listening to my ideas. Most importantly I would like to thank myself for giving myself the opportunity to make a difference in the world. This work is purely dedicated to the betterment of humanity.

ACKNOWLEDGEMENTS

I would like to thank Pavement Technology, Inc. for supporting this research program and making all of this possible. I would also like to thank the local companies in Bryan/College Station, TX: Red Ball Oxygen Co., Inc., Praxair or Linde Gas and Equipment, Brazos Valley Welding Supply, Bryan Hose and Gasket, and many more.

CONTRIBUTORS AND FUNDING SOURCES

Contributors

I would like to thank Dan Zollinger, Qi Ying, and Ying Li for assisting on this project. With their help I was able to create a clear correlation between the data and the products.

Funding Sources

I would like to thank Pavement Technology, Inc. for funding this project and supporting my role as a graduate assistant researcher.

NOMENCLATURE

α	absorption coefficient
B	magnetic flux density
c	speed of light in vacuum ($= 3 \times 10^8$ ms^{-1})
C	concentration of gas or material
D	electric flux density
$D_{p,n}$	diffusion coefficient for electrons (n) and holes (p)
e	charge of electron ($= -1.602 \times 10^{-19}$ C)
E	electric field, or electron energy
E_F	Fermi energy of an electron
E_g	bandgap energy
E_g	potential energy of an electron outside the surface forces
ε	permittivity of material
ε_0	permittivity of vacuum ($= 1/c^2\mu_0$)
ε_1	real part of the complex permittivity (dielectric constant)
ε_2	imaginary part of the complex permittivity
$f(E, T)$	Fermi-Dirac probability function
F	Fermi level or electrochemical potential
$g(t)$	generation rate of the electron hole pairs as a function of time ($g = \alpha I$)

$g(x)$	generation rate of electron hole pairs as a function of distance into the space charge layer
h	Planck constant ($= 6.63 \times 10^{-34}$Js) ($\hbar = h/2\pi$)
i	imaginary part ($= \sqrt{-1}$)
$i_{n,p}$	electron current density (n) and hole current density (p)
i_{ph}	photocurrent density
J_0, I, E_{rad}	light intensity or irradiance on semiconductor surface (W m^{-2})
k	reaction rate constant, imaginary part of the complex refractive index or adsorption index, and wave vector of Bloch function
k_B	Boltzmann constant ($= 1.38 \times 10^{-23}JK^{-1}$)
K	adsorption constant
L_D	Debye length in the semiconductor
$L_{n,p}$	diffusion length for electrons (n) and holes (p)
L_{SC}	thickness of the space charge layer in the semiconductor
ϕ	electric potential or quantum yield
λ	wavelength of light
m_0	rest mass of the electron
m_c, m_v	effective mass of the electron in conduction band or valence band
m^*	effective mass of electron
n	real part of complex refractive index
n_0	equilibrium concentration of electrons in semiconductor bulk
n_s	surface concentration of electrons

N_0	charge carrier density of semiconductor bulk induced by photos of energy E
N_A, N_D	concentration of donor (D) or acceptor (A) impurities in semiconductor bulk
N_c, N_v	effective density of quantum states in conduction (c) and valence (v) bands
ρ	charge density in material
p_0	equilibrium concentration of holes in valence band
p_s	surface concentration of holes
ppm	parts per million
r_{GAS}	oxidation percentage (GAS = NO, NO_2 but generally NO_x)
RH	relative humidity
σ	electrical conductivity of material
μ	magnetic permeability of material
μ_0	magnetic permeability of vacuum ($= 4\pi \times 10^{-7} \mathrm{Hm}^{-1}$)
X_m^n	ratio of the particles which possess n electrons and m holes in the volume V
U	external potential
U_{fb}	flat band potential
V	volume of TiO_2 particle
ν	frequency of electromagnetic wave
v	velocity of electromagnetic wave

ω	angular frequency ($= 2\pi\nu$)
ω_p	plasma frequency
w_T	thermodynamic work function

TABLE OF CONTENTS

Page

LIST OF FIGURES

Page

1. INTRODUCTION

TiO_2 in History, the Universe and Today

Titanium dioxide (TiO_2) is an oxide of titanium, and it has been used by humans for thousands of years. In the past humans have used TiO_2 mainly as white paint. It was identified in 1791 by William Gregor who used it in fine arts[48]. From there TiO_2 applications expanded to cosmetics, food, transistor and capacitor applications, nuclear chemistry and much more[49]. TiO_2 is very proliferant not only on earth but in many other places in the universe. TiO_2 and other titanium oxides have been found in asteroids, exo-planet atmospheres, stellar atmospheres and stars, and nebulas. The rocks brought back from the moon during the Apollo 17 missioned revealed a composition of up to 20% TiO_2[16]. TiO_2 may be a key player in the evolution of habitable planets due to the extremely long-term photochemical products such as oxygen[17]. One day the photochemical power of this material may help save Earth.

TiO_2 as a Photocatalyst and the Purpose of this Project

TiO_2 is one of the cheapest and most effective photocatalytic materials on the market[1,2]. This fact has led to abundant research on the topic with respect to TiO_2 and large-scale use of the material in industry as a photocatalyst and for water and air purification methods. TiO_2 is making an impact in the construction industry as a photocatalyst for the removal of pollutants but issues with effectiveness in the field are holding it back. These issues include but are not limited to durability, NO_x oxidation at varying TiO_2 concentrations, recombination and saturation, bandgap energy, photocurrent, space charge, and differential capacitance[10]. NO_x oxidation at varying TiO_2

concentrations is the main purpose of this study. With the data extracted from testing multiple TiO_2 concentrations at different input NO concentrations a master curve can be derived which provides the optimal TiO_2 concentration needed for a constant NO concentration in the sample atmosphere.

Outcome of Project

After analyzing the data, we were able to determine specific concentrations of TiO_2 needed for certain NO_x reduction percentages at a given NO concentration. This data allows industry to choose a specific TiO_2 concentration for a desired amount of NOx percent reduction assuming a constant NO concentration input. The data also shows certain TiO_2 mixtures, such as emulsions, have an impact on the gas reduction efficiency. Any material inhibiting the quantum source will have an impact on photocatalysis. A singular test ran in a N_2 atmosphere revealed the importance of O_2 in the photocatalytic reaction. Finally, a test will be performed with lab produced TiO_2 and it will be compared to the samples treated with P25 TiO_2 nanoparticles and TiO_2 paint from Amazon.

2. LITERATURE REVIEW

Introduction

The air we breathe is an invaluable resource that sustains life on Earth, but unfortunately, it's being increasingly polluted by a variety of harmful substances. Among the most common pollutants are SO_x, CO_x, NO_x, various acids such as HNO_3 and HCOOH, a multitude of complex hydrocarbons, and even radioactive species. These pollutants are constantly being released into the air by sources such as combustion machines and other industrial processes[12,13]. The impact of this pollution on the environment and human health cannot be overstated. It has led to the widespread degradation of ecosystems, caused respiratory problems and other health issues, and contributed to climate change through the release of greenhouse gases. As such, it is essential that we take action to reduce or eliminate the production of these pollutants. Fortunately, there are various methods available for air purification. For indoor applications, common methods include mechanical filtration, activated carbon, UV light, and ozone generators. These technologies work by removing or destroying pollutants at the source, thereby improving indoor air quality, and reducing the risk of health problems. However, outdoor air purification is a more complex challenge, as the air is constantly being exposed to pollutants from a variety of sources. To address this challenge, a range of technologies are used, including absorption, adsorption, condensation, and combustion[41,42]. These techniques work by capturing pollutants or breaking them down into less harmful compounds, but they are often less effective than indoor solutions due to the sheer volume of pollutants in the air. Air pollution is a

serious problem that requires urgent action. By implementing effective air purification technologies and reducing the production of pollutants at their source, we can make a clean tomorrow.

Is NO_x Bad or Good?

NO_x, which stands for nitrogen oxides, is a chemical compound that is formed from the combination of NO and NO_2. These gases are produced during the combustion of fossil fuels, such as in cars, trucks, and power plants[6-8]. High concentrations of NO_x are known to be harmful to both human health and the environment. Exposure to high levels of NO_x can cause respiratory problems, aggravate asthma, and even lead to premature death. However, it is important to note that NO_x is not inherently dangerous. In fact, in a clean troposphere, the concentration of NO is typically around 0.01-0.05 ppb, while the concentration of NO_2 is around 0.1-0.5 ppb[19]. These low levels of NO_x are actually beneficial to the environment, as they can help regulate the Earth's temperature and prevent the buildup of harmful greenhouse gases. It's worth noting that NO_x is not solely produced by human activities. Nature also produces NO_x in several different ways, with one of the most prominent being lightning[43]. When lightning strikes, the high voltage can ionize diatomic nitrogen and oxygen, causing them to recombine and form NO_x. Furthermore, NO has a positive impact on human health, as it acts as a vasodilator[44], which means that it helps to relax blood vessels and improve circulation. This has important implications for conditions such as hypertension and cardiovascular disease.

While NO_x can be both good and bad, it's essential to manage its production and exposure to protect human health and the environment. By taking steps to reduce emissions from combustion machines and supporting natural processes that produce NO_x, we can work towards a cleaner, healthier future for all.

Methods for Air Purification

In recent years, air pollution has become a major concern for people all around the world. With the increase in industrialization and urbanization, the air we breathe is becoming more and more contaminated with harmful particles and pollutants[45-47]. As a result, the need for air purification methods has become more pressing than ever before. In this regard, Roy et. al. has explained the methods of modern air purification and described the effectiveness of such. The application of mechanical filters is still a large part of the air purification scene, especially for indoor air purification. These air purifiers with mechanical filters have electrostatic precipitators which help remove particulates from the surrounding atmosphere. However, it is important to note that these electrostatic precipitators can be dangerous due to the production of ozone, which can be harmful to humans. Another method of air purification that has obtained mass attention is the use of activated carbon. The governing principle of activated carbon is adsorption; the large surface area and high porosity give a large probability for particulate extraction. Thus, activated carbon acts as a filter via physical adsorption and chemisorption. This makes it an effective method for removing pollutants such as volatile organic compounds (VOCs) and gases like carbon monoxide from the air.

Air can also be purified with UV light. The UV light will induce a voltage in the radiated material, thus killing pathogens or microbes present in the air. This method is especially useful in hospitals and laboratories, where the air needs to be free of harmful bacteria and viruses. Nano-fiber sheets made of polymer can also be used to extract particulates in the atmosphere via adhesion of particles. These sheets have a high surface area and can capture even the smallest of particles. This makes them an effective method for removing pollutants such as pollen, dust, and pet dander from the air. Photocatalytic materials are also of interest for air purification due to their ability to perform redox reactions. These materials use light energy to break down pollutants into harmless compounds. This method is effective in removing harmful gases such as nitrogen oxides and sulfur dioxide from the air. Finally, membranes made of soy proteins can be used to extract particulates via electrostatic force of attraction or dipole attractions. Soy protein isolate is generally used due to its high volume of proteins. These protein particles can be up to 50 microns in size and are effective in capturing pollutants such as dust, smoke, and bacteria. In conclusion, the methods of modern air purification are diverse and effective in removing harmful pollutants from the air we breathe. Each method has its advantages and disadvantages, and the choice of method depends on the specific needs of the user. As air pollution continues to be a major concern for people all around the world, the development of new and innovative air purification methods will continue to play a vital role in ensuring clean and healthy air for all.

Motivation

In recent years, TiO_2 has gained significant attention in the field of photocatalysis due to its remarkable properties such as high surface area, chemical stability, and low toxicity. Photocatalysis is a process that involves the use of a catalyst, such as TiO_2, to initiate a chemical reaction using light energy[11]. One of the key applications of photocatalysis is the removal of pollutants from the environment, particularly the elimination of nitrogen oxides (NO_x) from the air we breathe. Several studies have been conducted to investigate the photocatalytic capabilities of TiO_2 and TiO_2 doped materials for the oxidation of NO_x[9]. These studies aim to determine the extent to which TiO_2 can be used as a catalyst to remove NO_x from the environment. The researchers track the mass and sometimes the concentration of their samples to determine the efficiency of the TiO_2 catalyst[28-40]. However, it has been found that there is no clear correlation between the concentration of TiO_2 and the percentage of NO_x oxidation. This is because the studies that have been conducted so far have not provided results for samples with varying rates of TiO_2. Therefore, it is difficult to establish a definitive relationship between TiO_2 concentration and NO_x oxidation percentage. Despite this, the results of these studies have shown that TiO_2 and TiO_2 doped materials are capable of removing NO_x from the environment. The process of photocatalysis involves the absorption of light energy by TiO_2, which excites electrons from the valence band to the conduction band, leaving behind positively charged holes. These holes can react with water or oxygen molecules to produce hydroxyl radicals or superoxide ions, respectively. These reactive species can then oxidize NO_x to form harmless products such as nitrogen gas

and nitrate. In conclusion, TiO_2 and TiO_2 doped materials have shown great potential in the removal of NO_x from the environment through photocatalysis. While there is currently no clear correlation between varying TiO_2 concentrations and NO_x oxidation percentages, the results of these studies suggest that TiO_2 is a promising catalyst for environmental remediation. Further research is needed to establish a definitive relationship between varying TiO_2 concentration and NO_x oxidation percentages and to optimize the use of TiO_2 in the field.

3. EXPERIMENTAL SETUP AND MATERALS

Experimental Setup

All of the tests performed in this project follow these same procedures; there are no tests in this study which deviate from these procedures. The items used in this study are: Thermofisher 42i chemiluminese analyzer, Environics 4040 gas mixer, a three gallon stainless steel chamber (cyclindrical chamber with glass lid), a 120W LED with an output wavelength of 375 nm, a 30V 10A variable power supply for the LED, and various gas tanks including N_2, NO + zero grade air, and zero grade air. The RH is controlled by placing 800 mL of water in the chamber.

Figure 1

Experimental setup

Above are all the listed items which are used in this project. The LED can be seen on the bottom right of Figure [1] attached to a large heat sink. This LED is extremly efficient in oxidizing the NO_x due to the LED frequency closely matching the frequency found in equation **(1)** using the bandgap energy for TiO_2. The input gas in this experiment is not recycled back into the chamber. This is a simple flow through reactor. The schematic for ther experimental setup is below:

Figure 2

Flow Diagram of Experimental Setup

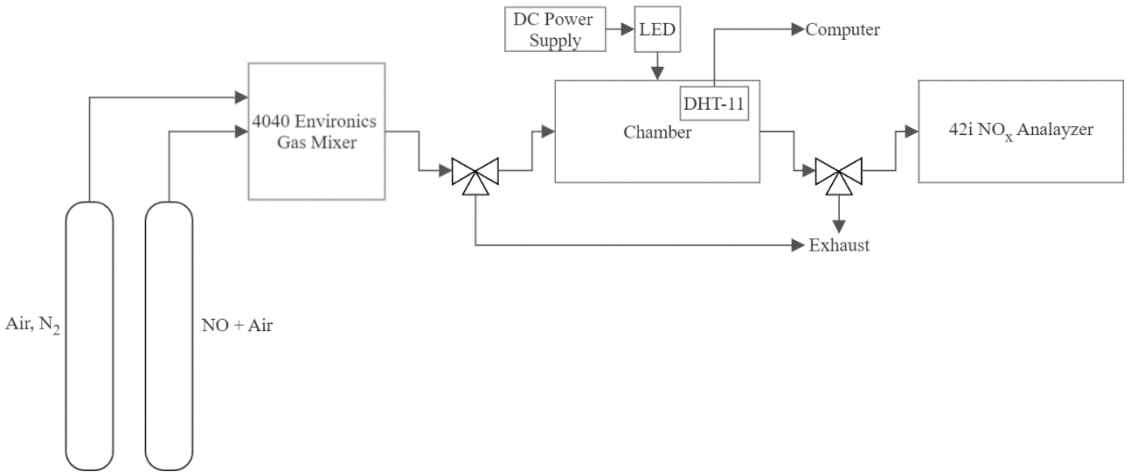

Note. The first three-way valve has an analog regulator and the exhaust is a vent hood

The gas tanks are connected to the 4040 Environs unit. This gas mixer allows the user select a target concentraion and flowrate. The selected gas concentration and flowrate are then fed into a three way valve which has an analog flowmeter connected to the inlet of the three way valve. This allows the user to select flowrates which may not be provided by the 4040 Environics unit. The selected concentration and flowrate are then

fed into the chamber where the selected sample is located. The output flow from the chamber is then exhausted, and the vacuum pump from the 42i NO_x analyzer draws only what it needs. The power supply given an constant power input to the LED. The quantum flux from the LED is directed into the chamber. The DHT-11 sensor is placed om a breadboard which is glued to the interior of the chamber. The Arduino is also attached to the breadbaord inside the chamber. A hole was drilled into the chamber and the cord was inserted into the chamber for power and control of the sensor. The cord was caulked closed to ensure the chamber did not leak. The cord can actually be seen in Figure [2] on the right side of the chamber. The computer used to collect data from the DHT-11 sensor is played atop the 42i in the picture; this is the general procedure for testing. The samples are ~10" from the LED. The lid on the chamber is glass. The following procedure is how all samples were tested:

1) Power on all devices and allow Thermofisher 42i to attain proper temperature (allow to heat up for 30 minutes)
2) Add 800 mL of water to the chamber
3) Insert sample into chamber and clamp the glass lid
4) Open the appropriate gas tanks and program the Environics 4040 to the desired settings
5) Charge the chamber for a minimum of 11 minutes to replace the atmospheric gas in chamber (the residence time of the gas in this chamber at 1 LPM is approximately 11 minutes)

6) After chamber has been charged with the test gas the test can begin (stop the gas flow and restart it before starting the test); place the LED above the chamber and plug the LED into the power supply
7) Open the Arduino robot program for the DHT-11 sensor and begin taking readings in the serial monitor for RH and temperature
8) The test is a two hour test: first hour the LED is off and for the second hour the LED is on
9) Obtain the NO_x concentration values every 10 minutes or extract the data from the Thermofisher 42i at the end of the test
10) Power off all devices when complete and be sure to close the gas tanks
11) The only values of interest are the NO_x values at the one-hour and two-hour mark; the oxidation percentages are obtained from these two experimental values

The following parameters are kept constant throughout the entire testing procedure: flowrate, NO concentration, power to LED, RH, and mass and/or concentration of TiO_2. The flowrate is always kept at 1 LPM aside from a singular test. The input NO concentration varies from 0.5 to 10 ppm as will be explored in the results section. The RH in the experiment does fluctuate due to the change in temperature introduced by the LED at the one-hour mark. Due to cost the 800 mL of water added to the bottom of the chamber is the only way to reliably add water to the reaction. A plot of the RH will be included in the results section along with the temperature change. These readings were recorded with a DHT-11 sensor and an Arduino (both are placed inside the chamber). This procedure is based on the JIS R 1701-1 standard used in Japan[26]. All. the

concentration values for the TiO_2 samples are taken with the Niton^{TM} XL3t XRF analyzer used in the "soils" mode.

Materials

The materials used in this project are either pure TiO_2 particles of varying diameter or emulsion products containing these P25 TiO_2 nanoparticles provided by Pavement Technology, Inc. A TiO_2 paint from Amazon is also tested. Our lab also successfully created TiO_2 nanoparticles which were tested for efficiency. All the materials mentioned can be seen below using electron microscopy.

Figure 3

P25 TiO_2 nanoparticles provided by Pavement Technology, Inc.

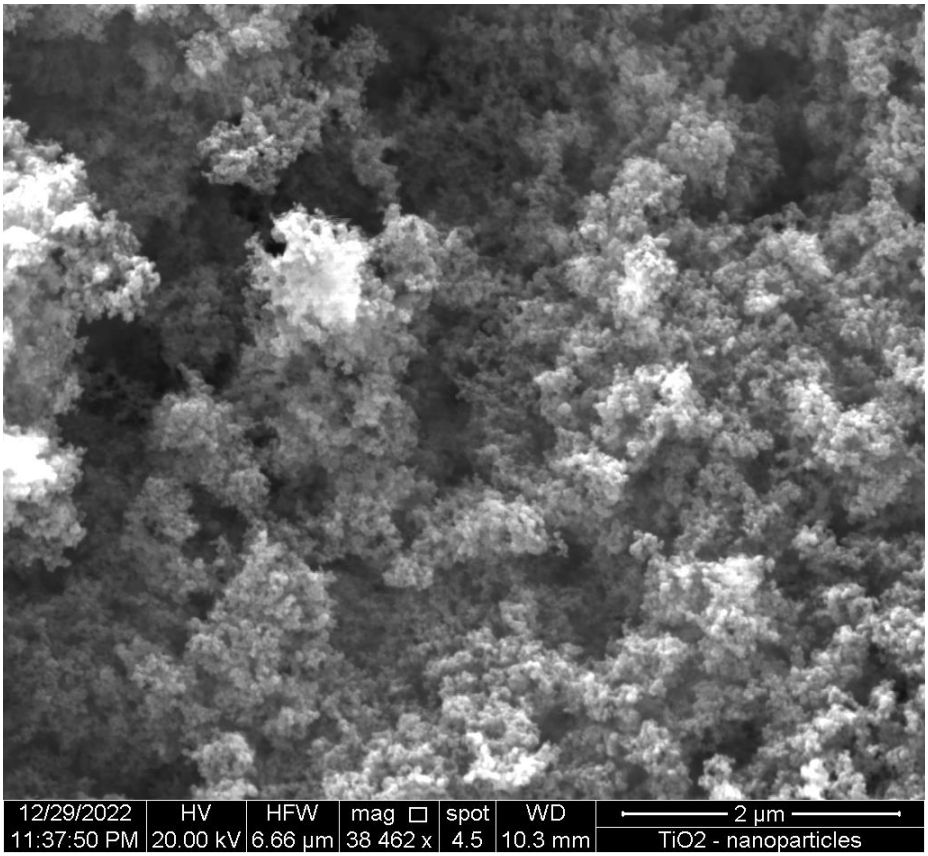

Above are the nanoparticles used in the emulsion products (these TiO_2 nanoparticles are also used without the emulsion). The images were taken with the FEI Quanta 600 FE-SEM at the Texas A&M microscopy and imaging center. The TiO_2 spheres are difficult to see in Figure [3] as the limit of the FEI Quanta 600 FE-SEM are being pushed.

Figure 4

TiO_2 paint from Amazon

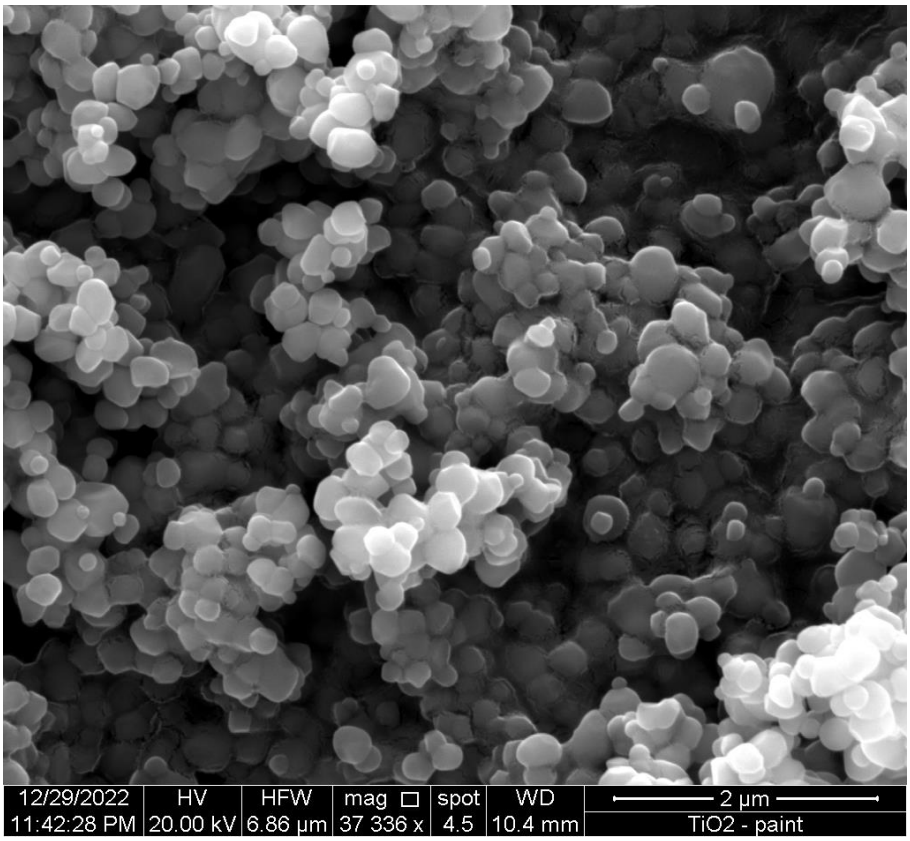

In Figure [4] the TiO_2 paint can be viewed. The particles are much larger than the nanoparticles in Figure [3] thus explaining the price difference. During this project our team created TiO_2 nanoparticles by using Ti electrodes and a thermal plasma (an old DC welding circuit). These nanoparticles can be seen in Figure [5].

Figure 5

Lab produced TiO_2 nanoparticles via thermal plasma and Ti electrodes

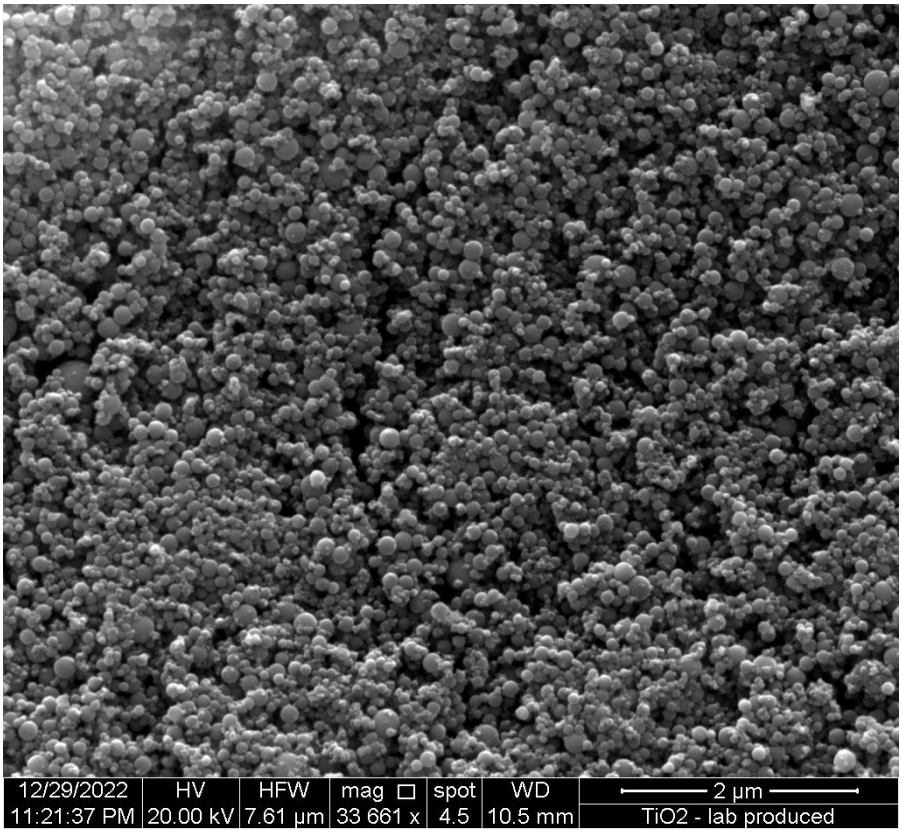

These TiO_2 nanoparticles are not quite as small as the TiO_2 nanoparticles provided by Pavement Technology, but they are much smaller than the TiO_2 paint. These images allow for the unique geometry of the TiO_2 to be viewed.

4. RESULTS

Zero Tests (no TiO_2 in chamber) and Calibration Tests

To validate the testing procedure a zero test must be performed i.e., a test with no TiO_2 in the chamber. Below is a zero test with the following parameters: 1 LPM flowrate, 1 ppm NO input mixed with zero grade air, 120W drawn by the LED, an average RH of 77.5%, an average temperature of 26.5°C and no TiO_2. Below in Figure [6] the zero test can be seen.

Figure 6

Zero test with light – 120W, 1 LPM, 1 ppm NO, RH_{avg} = 77.53%, T_{avg} = 26.52°C

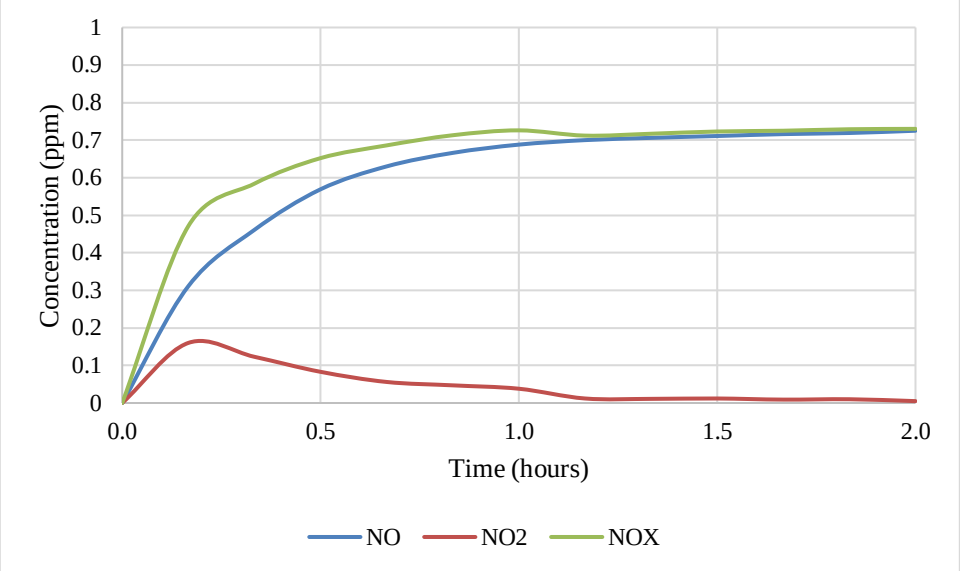

Here the NO concentration steadily rises as a logarithm with time (regardless of the photonic yield) and the NO_2 diminishes over time because there is no TiO_2 to generate NO_2. Also, the quantum flux can break the NO_2 down into NO (equation (**66**)) which may also be a reason for the low NO_2 concentration after the 1-hour mark. If there was

TiO_2 in the chamber, then NO_2 would be produced by the photochemical reactions seen in equation **(10)**. Below the plots of the RH and temperature can be seen over time.

Figure 7

RH data of zero test with light

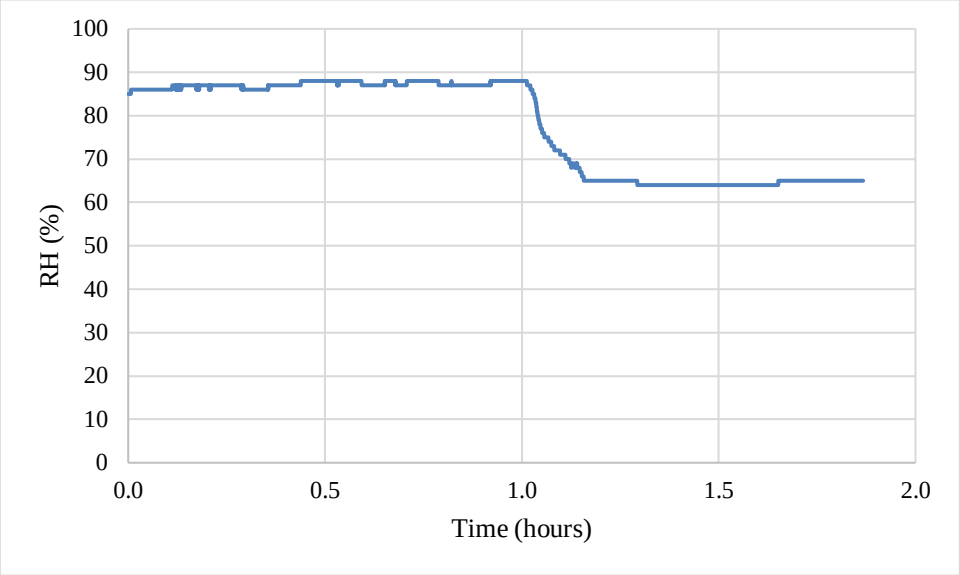

When the LED is powered on the temperature of the atmosphere inside of the chamber can be seen to rise. Conversely the RH drops as the temperature increases. This is consistent with all the tests. The tables in Appendix B contain average temperature and RH values; these are the averages of the plots seen above for each respective test.

Figure 8

Temperature data of zero test with light

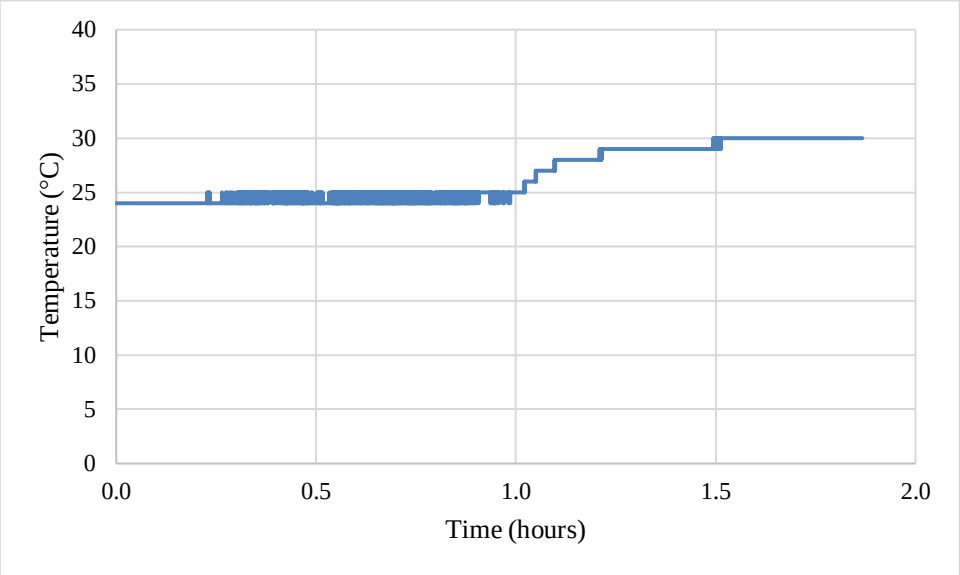

Next a zero test without using the light was tested in order to observe the maximum concentration of NO which can be achieved in the chamber. This test can be seen below:

Figure 9

Zero test without light – 0W, 1 LPM, 1 ppm NO, RH_{avg} = 82.07%, T_{avg} = 23.59°C

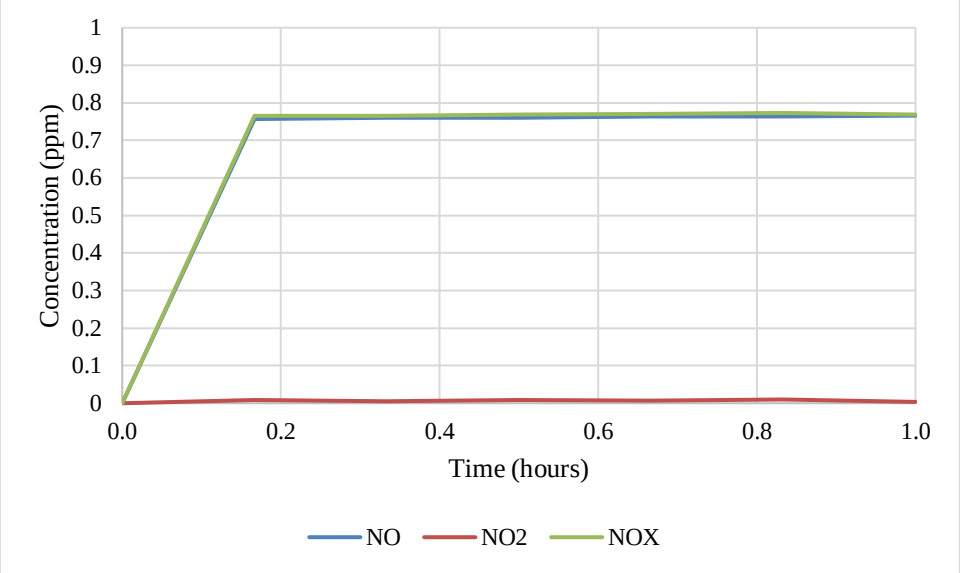

There is no change in concentrations due to no light and no TiO_2 inside the chamber. The standard deviations of the steady state concentration values for NO, NO_2 and NO_x are 0.0031, 0.0023, and 0.0026 respectively. The span gas was introduced into the chamber for 20 minutes before the test in order to replace the gas inside the chamber and to establish the span gas concentration (1 ppm NO) inside the chamber. Below the RH of the test can be seen:

Figure 10

RH data of zero test without light

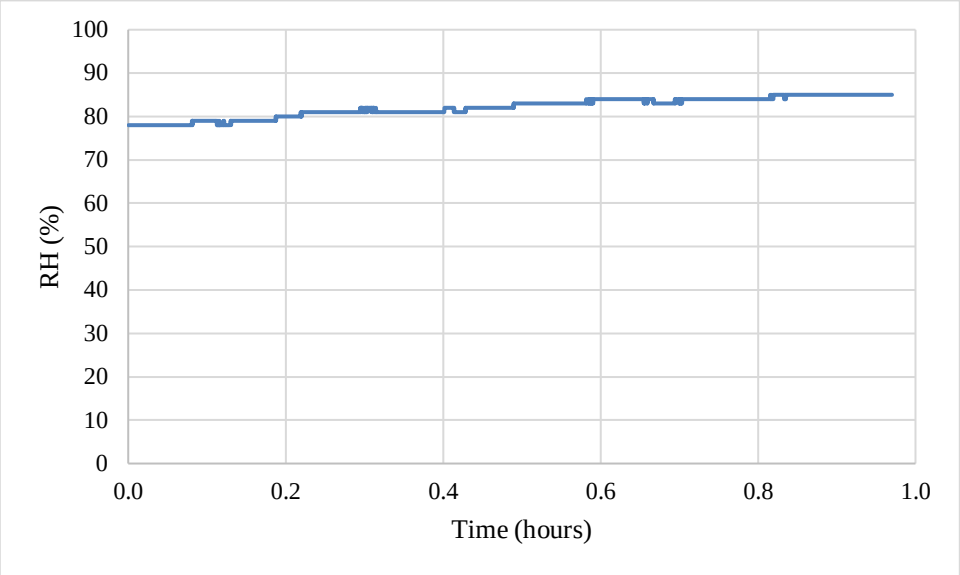

The RH and temperature are fairly constant throughout the test. The RH does increase with time; this is due to the RH not being controlled in the experiment. Below the temperature of the test can be seen:

Figure 11

Temperature data of zero test without light

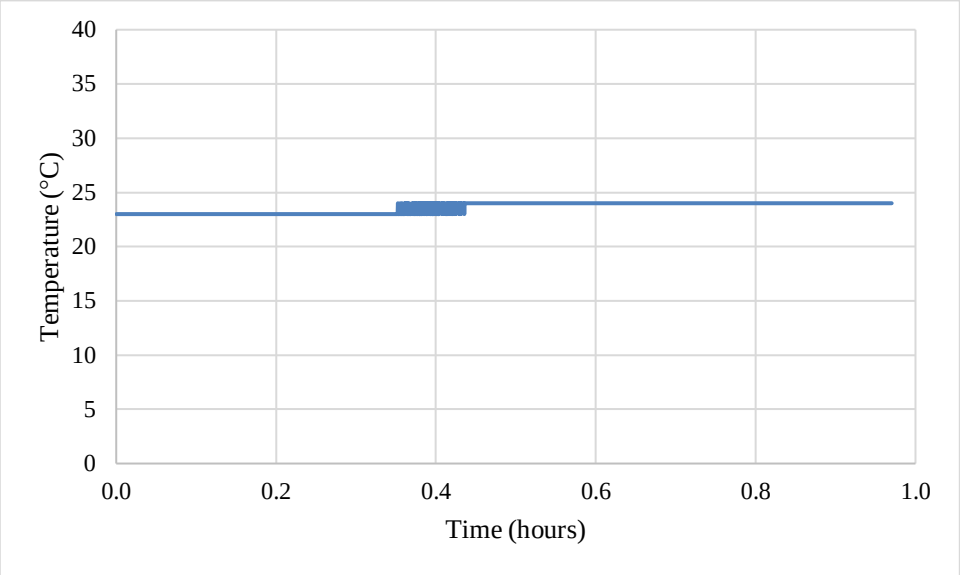

Concluding this test another test was performed to calibrate the experimental program and prove the validity of the results by tight grouping of the NO concentration values (the only input concentration which is controlled in the reaction). A test was run at 10 minute intervals with the LED on and off at each interval. The input flowrate is 2 LPM and the input NO concentration is 1 ppm. The RH and temperature plots will be provided with the hope of giving clarification to the NO_2 concentration throughout the test. The sample used in this test was F1, the first sample in set F. Below is the calibration test:

Figure 12

Calibration test (sample used: F1)

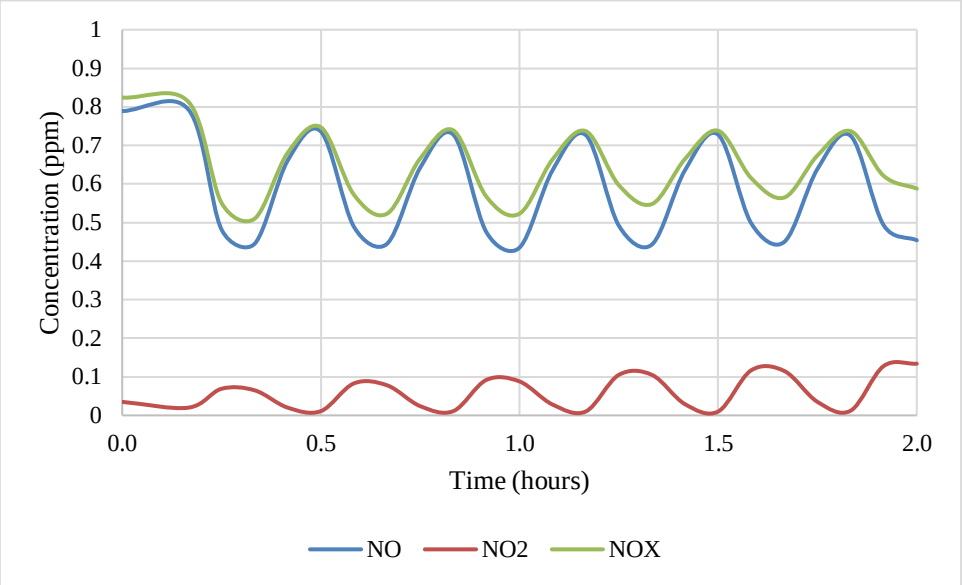

The standard deviation of the maxima NO concentrations in the figure above is 0.001224 and the standard deviation of the minima NO concentrations is 0.007228. This test proves the reliability of the readings via repeatability. It should be noted the span gas was supplied into the chamber for at least 20 minutes before the start of the test as can be seen in the beginning of the figure thus allowing the concentration to reach a maximum value. After this the intervals of the LED on and off was initiated. Below the RH of the calibration test can be seen:

Figure 13

RH data of calibration test

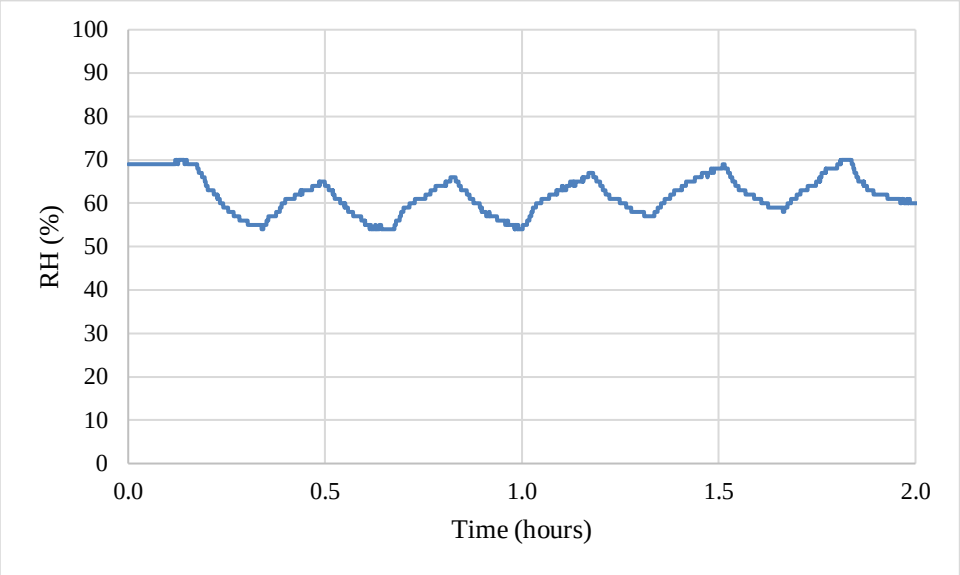

The RH matches the oscillation of the quantum flux extremely well. With the introduction of the quantum flux the RH decreases due to the temperature increase. Below is the temperature data for the calibration test:

Figure 14

Temperature data of Calibration test

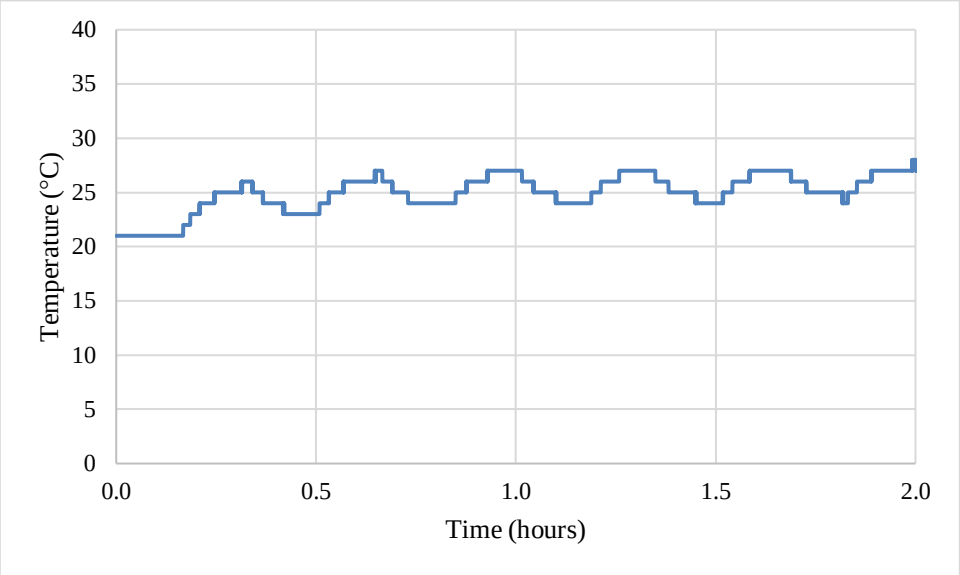

Tests with High Concentrations of TiO_2 (sets E, F and H)

The series' to be considered here are set E, set F, and part of set H from the database. The masses of these samples are known as well as the concentrations in ppm except for set E; for set E only the TiO_2 concentration is known in ppm. For samples F1, F2 and F3 (the first character is the set name, and the second character is the sample number) the masses of TiO_2 are 0.0039, 0.0592, and 0.0138 grams respectively; the corresponding concentrations for these samples are 118800, 122800, and 242500 ppm respectively. For samples H1, H2 and H3 the masses of TiO_2 are 0.05, 0.1 and 0.25 grams respectively; the corresponding TiO_2 concentrations for these samples are 57400, 100333 and 198666 ppm respectively. For set E we have E1, E2 and E3. The corresponding concentrations for these samples are 573400, 573800 and 253667 ppm respectively. For set F the input NO concentrations are 2, 5 and 10 ppm. For set H the

input NO concentration is only 1 ppm. Set E has NO input concentrations from 0.5 to 2 ppm. Set E is notable different in that the power input to the LED is only 50W as opposed to the other tests which are at 120W. There are two key points related to increasing the input NO concentration which will be noticeable in the results: the production of NO_2 increases and the NO_x oxidation percentage decreases due of the former. Below in Figures [16-18] the concentration plots over time can be seen for F1. All the other input parameters follow the parameters established in the experimental setup and materials section. The equation used to calculate the oxidation percentage is as follows:

$$r_{GAS} = \frac{C_{1\ hour} - C_{2\ hour}}{C_{1\ hour}} \times 100 \quad \textbf{(84)}$$

Where r is the oxidation percentage of the gas, C is the concentration of the gas, and GAS is either NO, NO_2 or NO_x. The figures are labeled with the power supplied to the LED, flowrate, input NO concentration, RH, and temperature data.

Figure 15

E1 – 50W, 1 LPM, 1 ppm NO, no RH and temperature data

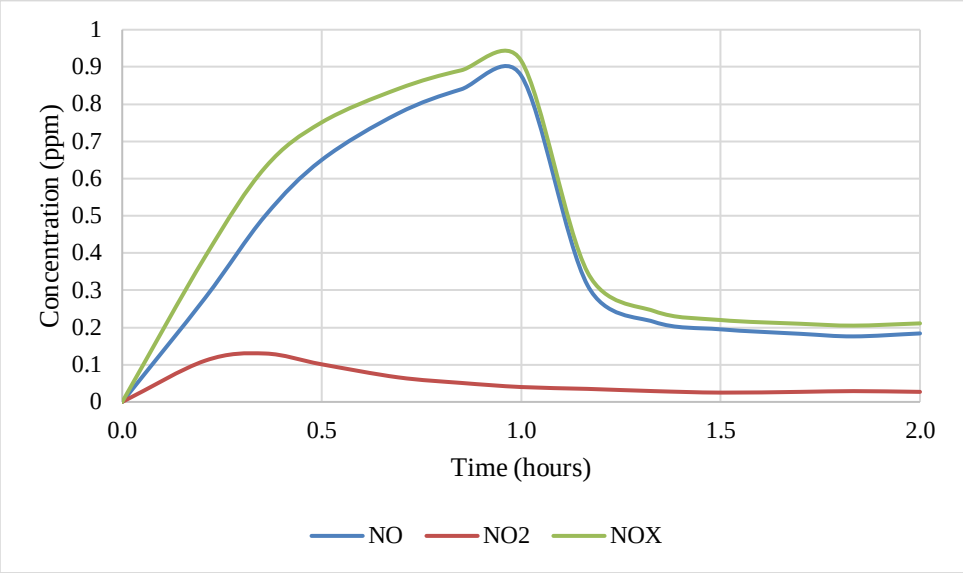

Here only E1 is shown and the rest of set E are in Appendix A. E1 and E2 do not have water in the chamber and this is evident in the maximum NO concentration. When there is water in the chamber the general threshold for the NO concentration is ~0.8 ppm as can be seen in the zero tests. The tests for E1 and E2 are extremely similar which inspires confidence in the results obtained. The NO_2 concentration does not change much due to the low NO concentration input. We will see later the NO_2 production increases with an increase in the input NO concentration.

Figure 16

F1 – 120W, 1 LPM, 2 ppm NO, RH_{avg} = 70.76 %, T_{avg} = 25.56°C

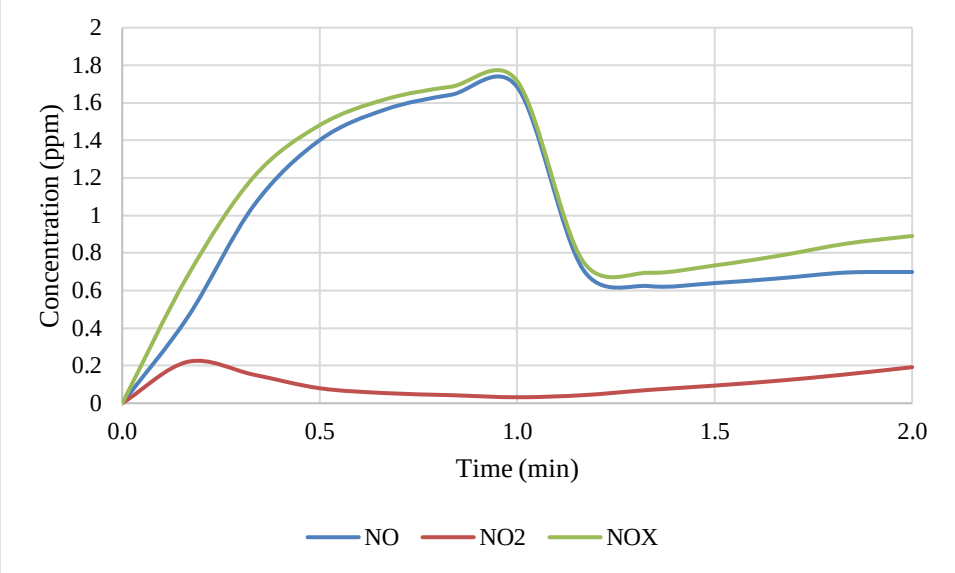

The F set is a unique set which explores the possibilities of high input NO concentrations. As other studies have shown the amount of NO_x oxidized increases as the input NO concentration increases but the percentage of NO_x oxidized for that span gas decreases[1-4]. This can be clearly seen with the F1 sample tested at 2, 5, and 10 ppm NO. In Appendix A the remaining tests for set F can be found which further prove the argument. The tests with F1 were selected specifically because over time the NO_x dissolve into the water thus completely controlling the production of NO_2 as can be seen with the tests with F3. It is not completely known as to why the NO_2 concentration is completely controlled but the assumption of the dissolved NO_x into the water seems most probable. The Henry's gas law constant for NO_x species is low but the dissolved NO_x and possibly dissolved ozone play a huge role in the experiments over time as can be seen with set F.

Figure 17

F1 – 120W, 1 LPM, 5 ppm NO, RH_{avg} = 74.82%, T_{avg} = 25.25°C

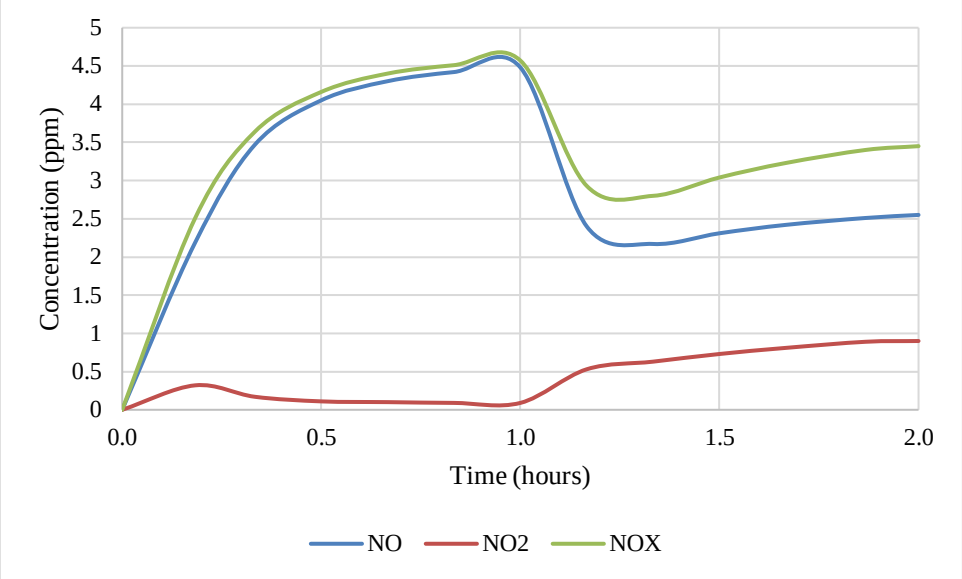

Here the production of NO_2 can be seen to increase as the input NO concentration increases. Also, the oxidation of NO_x decreases as the input NO concentration increases. This will be further evident in the following figures for F2 and F3. With F2 there is more TiO_2 available than F1 (F2 has a mass ~15 times larger than F1) thus resulting in a larger total current through the irradiated semiconductor.

Figure 18

F1 – 120W, 1 LPM, 10 ppm NO, RH_{avg} = 70.83%, T_{avg} = 24.96°C

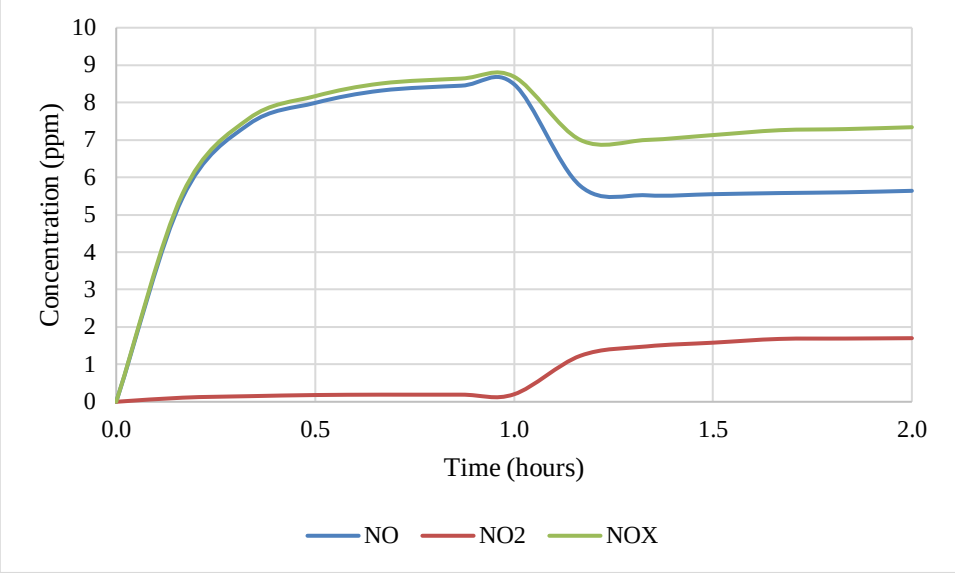

What must be noted about this testing is the NO_x dissolving into the 800 mL of water. All the tests with F3 can be seen to produce less NO_2 than the tests with F1 and F2. This is directly related to the dissolved NO_x in the 800 mL of water because F1 and F2 samples were tested before F3. Thus, the dissolved NO_x in the 800 mL of water directly impacts the NO_x oxidation percentage. Tests with F1 thus have little to no impact from the dissolved NO_x and tests with F3 have high impact from the dissolved NO_2. Set F samples were tested with this in mind to determine how the 800 mL of water impacted the testing. The conclusion is the dissolved NO_x inhibits the formation of NO_2 gas thus only allowing the NO to exist in the chamber. The NO_2 in this experiment occurs via NO coming into contact with O_2 and other oxygen species, and the TiO_2 generated NO_2. Below are the plots for H1, H2 and H3. Again, the input NO concentration for all samples in set H are 1 ppm.

Figure 19

H1 – 120W, 1 LPM, 1 ppm NO, RH_{avg} = 65.37%, T_{avg} = 27.33°C

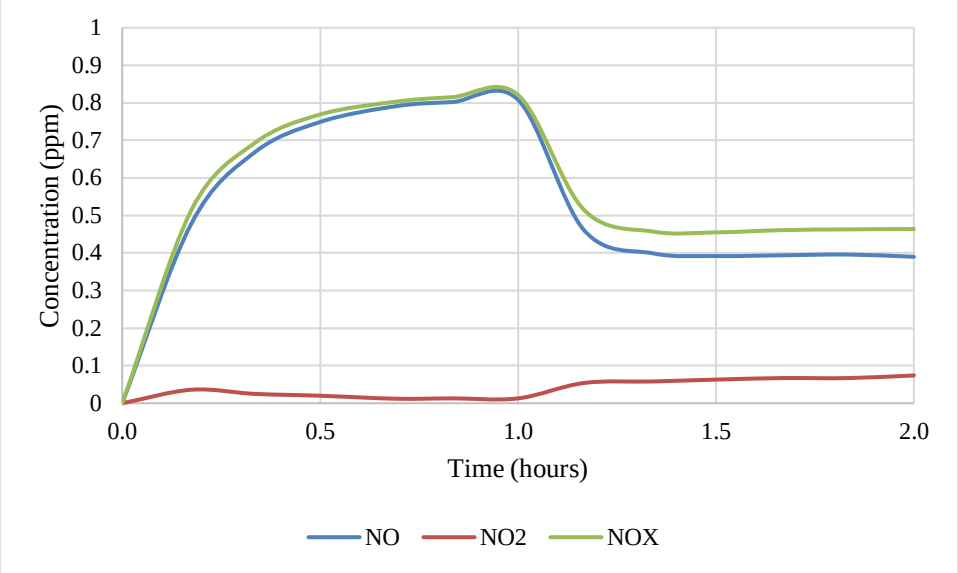

With set H the oxidation of NO_x is seen to be higher than set F due to the lower input NO concentration. The concentrations seem to find an equilibrium state much quicker than set F. The masses of set H are higher than set F thus resulting in the equilibrium states seen in the tests with set F The higher masses also correlate to a higher photocurrent due to the larger number of charge carriers. With a higher photocurrent we can expect the NO_x concentration to reach an equilibrium with the surrounding environment faster. With a lower input NO concentration, we see a higher NO_x oxidation percentage. Although as the input NO concentration increases the amount of oxidized NO_x increases with it even though the oxidation percentage decreases. Thus as the input NO concentration increases the potential amount of oxidized NO_x increases.

Tests with Low Concentrations of TiO_2 (emulsion samples and set H)

The emulsion products mentioned prior are used to treat asphalt roadways with TiO_2. The samples from these roadways are sent to our lab and are tested in the chamber. Due to the low concentrations found on the samples the photocatalytic performance is lower than the high concentration samples seen in the last section. Below are some tests which have been performed with samples pulled from treated roadways. The concentrations will be provided; no mass values are provided due to the low mass values on these samples. The mass values are not estimated due to the reliability of the Niton™ XL3t XRF analyzer. It must be noted that the Niton™ XL3t XRF analyzer is used in the "soils" mode only.

Figure 20

Edna, MN – Treated with ARA1-Ti Emulsion – 120W, 1 LPM, 1 ppm NO, RH_{avg} = 70.10%, T_{avg} = 24.51°C

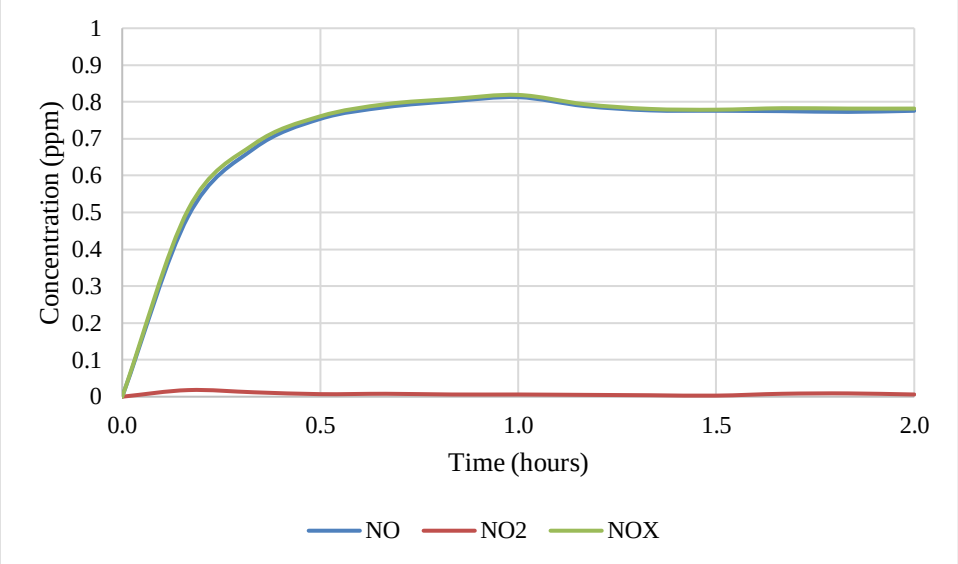

Figure 21

Charlotte, NC 9156.2 – Treated with ARA1-Ti Emulsion – 120W, 1 LPM, 0.5 ppm NO, RH_{avg} = 67.71%, T_{avg} = 24.32°C

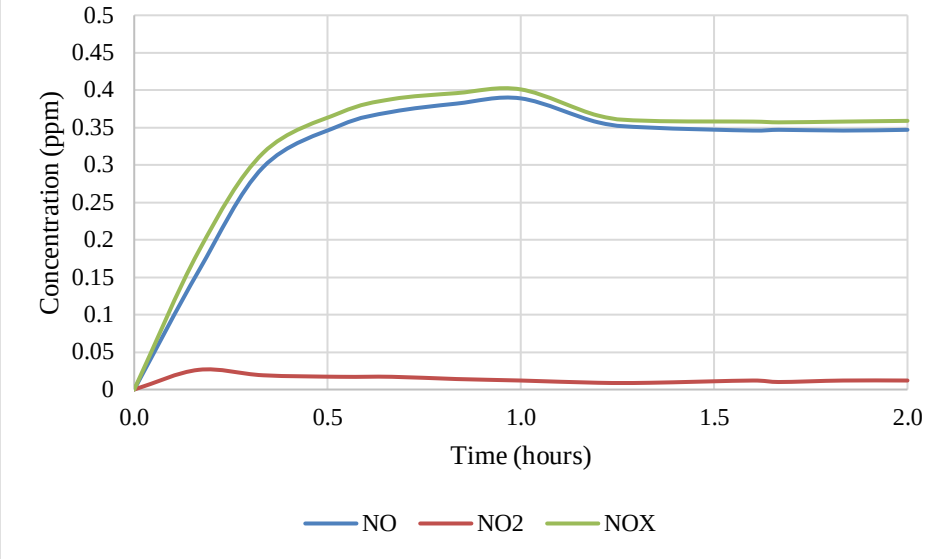

Both of the above figures show how the low concentration samples (4154 and 6751 ppm TiO_2 respectively for the two tests above) react in the chamber. Both yield low NO_x oxidation percentages due to the low concentrations of TiO_2. These data points of the Pavement Technology, Inc. samples are invaluable; they are direct proof of the correlation between TiO_2 concentration and NO_x oxidation percentage as will be seen in the master curve.

Figure 22

Charlotte, NC 8672.2 – Treated with ARA1-Ti Emulsion – 120W, 1 LPM, 1 ppm NO, RH_{avg} *= 64.89%,* T_{avg} *= 24.34°C*

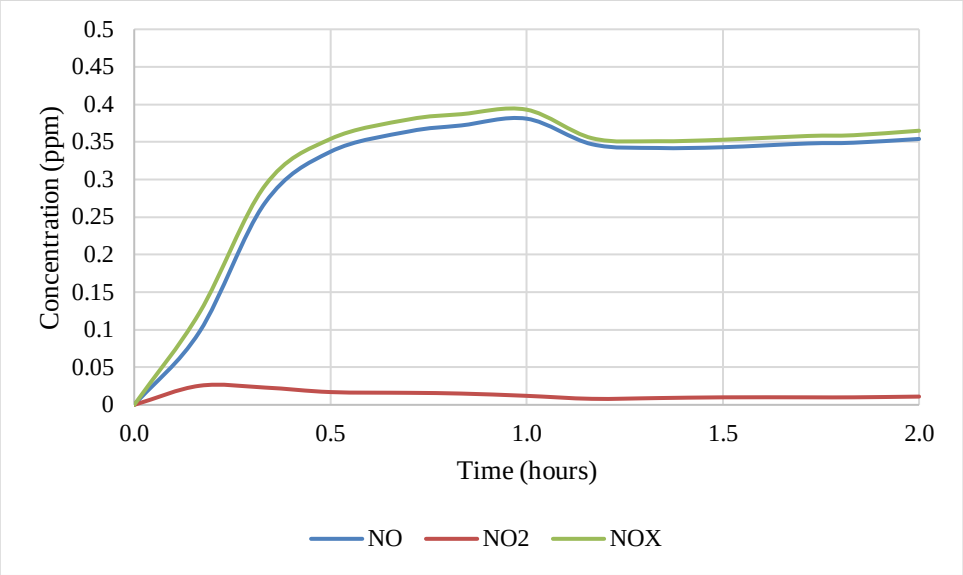

Figure [20] can be compared with H1, H2 and H3 concerning oxidation of NO_x. The concentrations of the samples used in Figures [20-22] are 3164, 6751 and 4154 ppm respectively. The low concentrations of TiO_2 are directly related to the low NO_x oxidation percentages. In Figure [21] and [22] the input NO concentration is changed to 0.5 ppm to obtain a larger NO_x oxidation percentage. Below are the plots for H4, H5 and H6 which are samples made with 0.05, 0.1 and 0.25 grams of TiO_2 respectively. H4, H5 and H6 are made in an ARA1-Ti emulsion mixture.

Figure 23

H4 – 120W, 1 LPM, 1 ppm NO, RH_{avg} = 64.36%, T_{avg} = 26.81°C

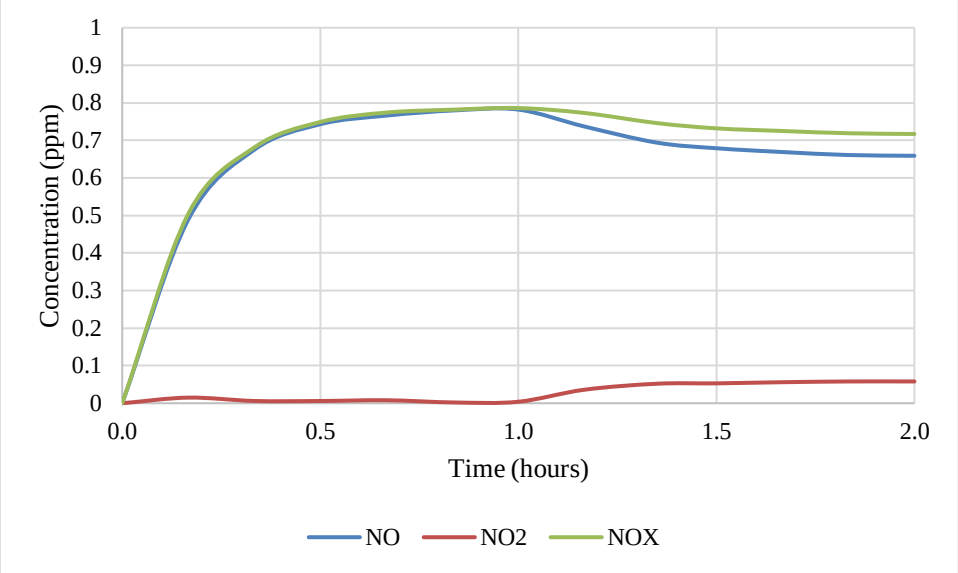

H4, H5 and H6 can be seen to oxidize much less than H1, H2 and H3. This is due to the emulsion absorbing a percentage of the photonic yield thus decreasing the total current in the semiconductor thus resulting in a lower NO_x oxidation percentage. This is more clearly viewed in Figure [26].

Figure 24

Comparison of emulsion products from Pavement Technology, Inc.

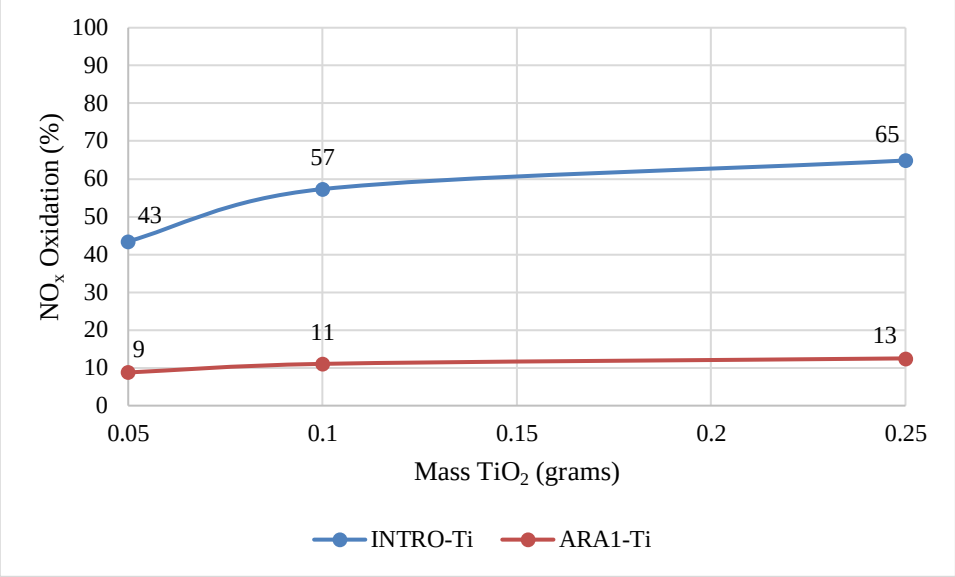

Note. These are tests H1-H6

The INTRO-Ti does not absorb nearly as many photons, in fact most of this carrier evaporates leaving just the TiO_2. The ARA1-Ti has a large amount of emulsion which does not evaporate thus blocking the photons from reaching the TiO_2. Below are images of the ARA1-Ti and INTRO-Ti respectively using the LEICA DM 6B light microscope.

Figure 25

ARA1-Ti + TiO_2 under microscope

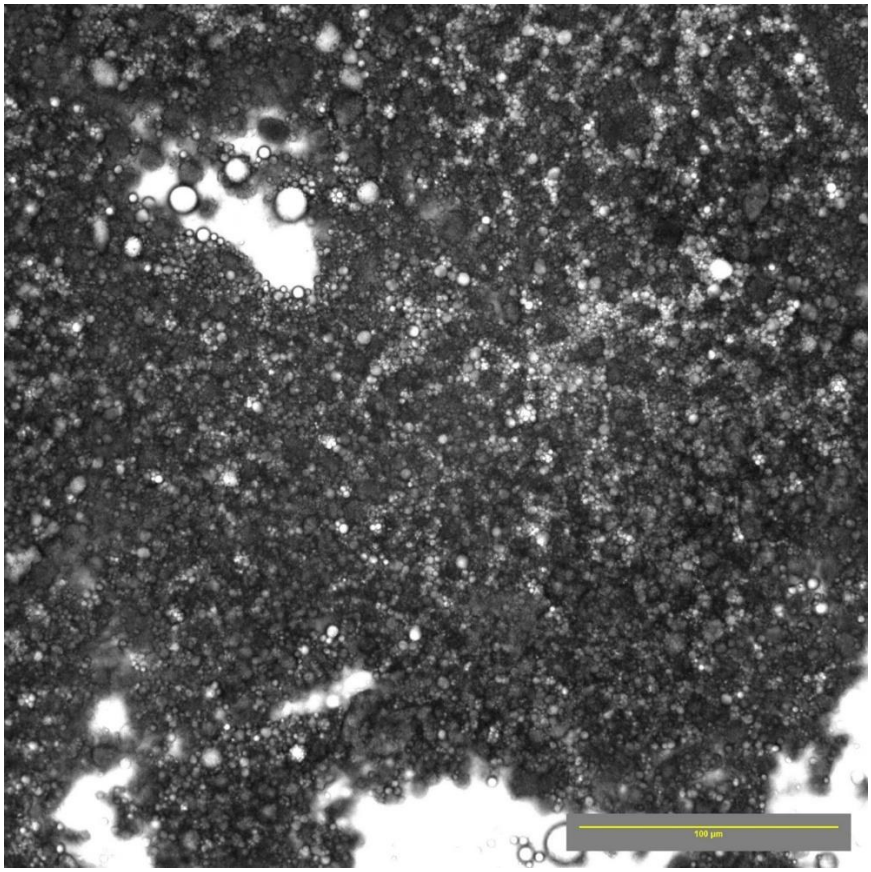

Note. The mixture is 50% ARA1-Ti and 50% TiO_2 by volume

Each sample is 50% carrier and 50% TiO_2 nanoparticles by volume. A small drop was used from each mixture and placed on a slide for inspection.

Figure 26

INTRO-Ti + TiO_2 under microscope

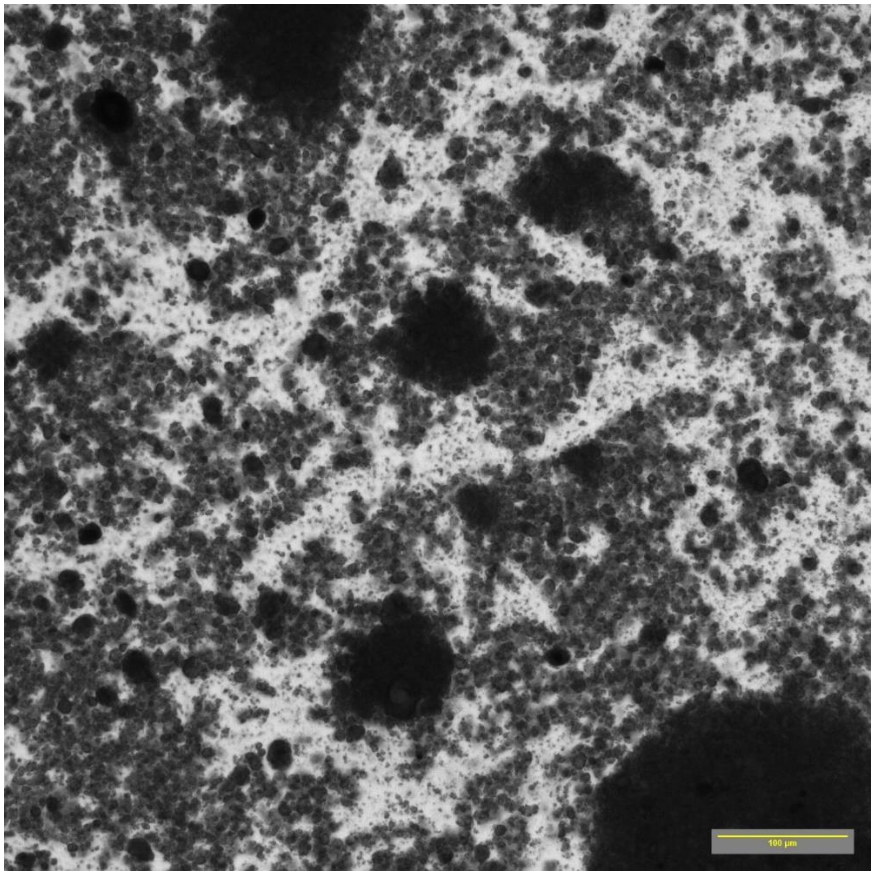

Note. The mixture is 50% INTRO-Ti and 50% TiO_2 by volume

Test in N_2 Atmospheric Environment

Sample F1 was tested in an atmospheric environment of N_2 and pure air + NO with an input NO concentration of 1 ppm. All the remaining parameters follow the guidelines in the experimental setup section. As mentioned previously the one drawback of using this experimental procedure is the NO_x which is dissolved into the 800 mL of water. In the prior tests the NO_2 production decreases as the NO_x dissolves into the

water, and the NO seems to be unaffected. In the pure N_2 atmosphere something interesting happened as can be seen below:

Figure 27

Nitrogen test – 120W, 1 LPM, 1 ppm NO, RH_{avg} = 59.49%, T_{avg} = 27.55°C

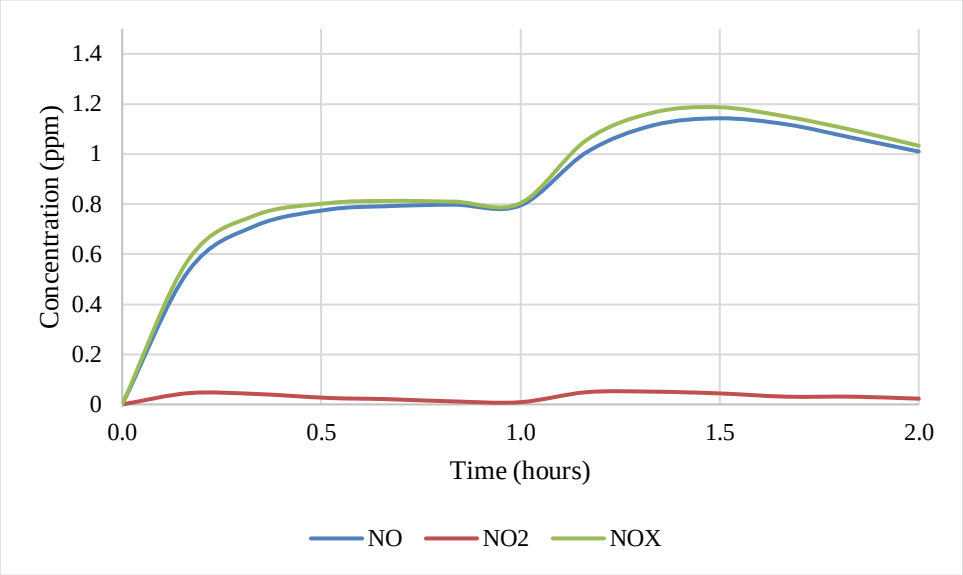

The production of NO_2 is minimal but the NO concentration increases with the introduction of the quantum flux (irradiation at 375 nm). This shows the important role a water body has in the production of NO_x in the absence of O_2. This response in concentration never occurred while O_2 was present in the chamber. It's as if the O_2 acts as a barrier which locks the dissolved NO_x to the water body. Without the O_2 barrier the dissolved NO_x is energized by the UV radiation thus returning the NO_x back into the chamber as a gas. In equations (a-b) NO_2, HNO_2, and NO_3 generate NO with an input frequency. Thus, if any of these chemicals are in the water body there is a probability they will be converted back to a gaseous state of NO. This unique result points to one conclusion: water bodies (including soils) can generate NO_x with the input of an

electromagnetic wave. This is especially true for urban areas where pollution is high. The transport of hydrocarbons and complex hydrocarbons into said water bodies provides a large soup of pollution which can enter the atmosphere as reduced gases upon irradiation. Future tests with this gas configuration should test different balances of N_2 and O_2 to establish the role of O_2 in this unique reaction.

Master Curve

This section is the concatenation of all tests and concentrations for deriving a curve which can predict how much NO_x can be oxidized under certain parameters. These parameters are flowrate of 1 LPM, an input NO concentration of 1 ppm, 120W drawn by the LED, and 800 mL of water added to the chamber for a constant flux of RH. Below are two plots which are the same curve but the second one is targeted on the beginning of the logarithm.

Figure 28

Master curve – 120W, 1 LPM, 1 ppm NO, RH and temperature vary

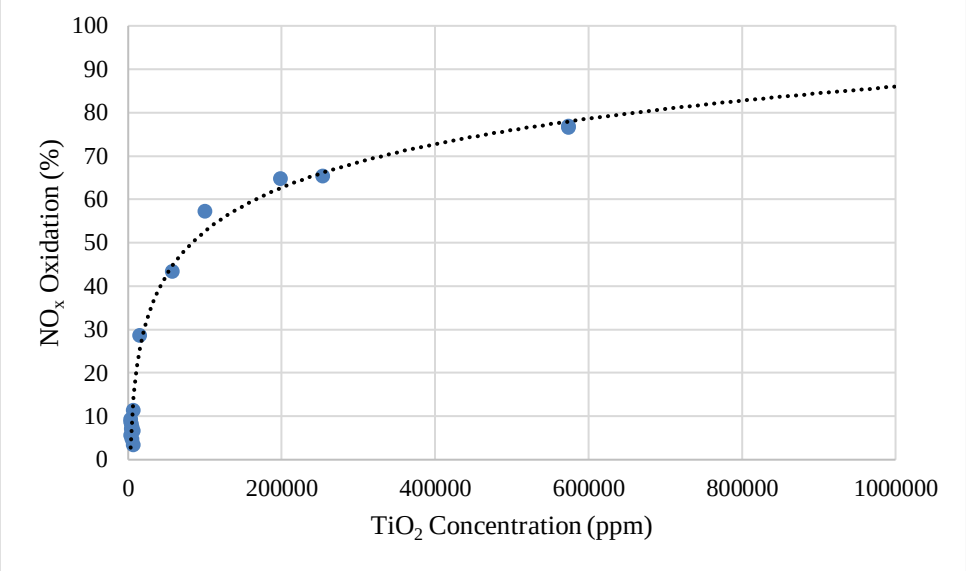

Figure 29

Master curve (beginning of curve) – 120W, 1 LPM, 1 ppm NO, RH and temperature vary

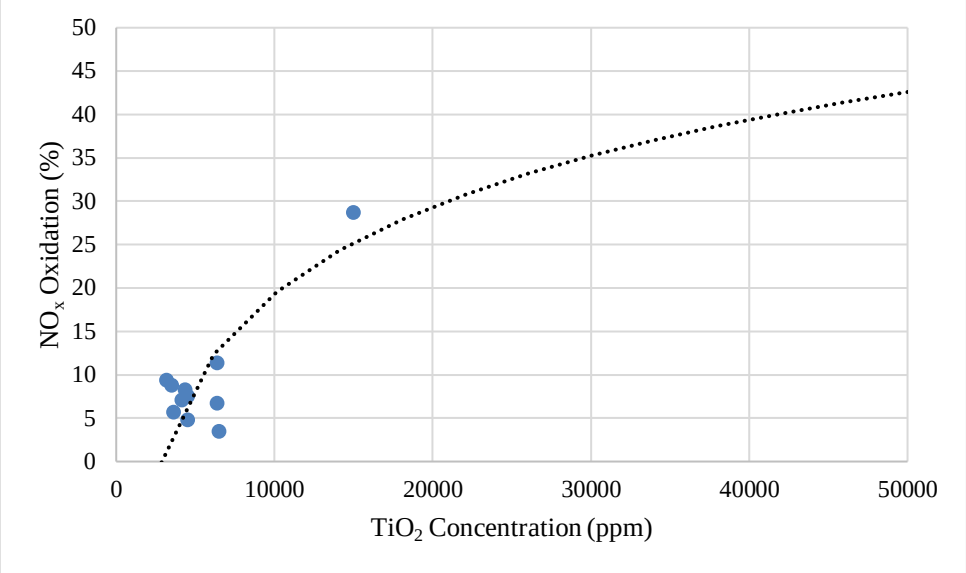

Note. Curve is the same the previous figure, but the x-axis is focused on the beginning With this curve an input TiO_2 concentration can be selected and under the parameters listed above the output NO_x oxidation percentage can be estimated. In Figures [27] and [28] it is obvious the points do not fall directly on the curve, but the curve is a great approximation of the possible output. The inaccuracy is directly related to the RH not kept constant throughout the entire test. This output value is heavily dependent on the NO_2 produced by the photochemistry thus any deviation from the norm of the NO_2 production will cause the output not to fall directly on the master curve. That said the master curve is an excellent predictor as all experiments under these listed parameters fall extremely close to the curve provided. The master curve follows a logarithm curve as seen above. The equation for the curve seen above is $y = 14.473\ln(x) - 113.96$ where x is TiO_2 concentration and y is the oxidation percentage of the input NO_x. This

equation follows all the parameters listed in the experimental setup section and does not represent any other conditions, parameters, environments, or tests. For all of those in the future it is highly recommended to test at different concentrations under certain constant parameters to obtain this curve. Once we start doping TiO_2 and other photocatalysts with superconductors we must create master curves for those and compare them to the master curves obtained with pure TiO_2.

Tests with Lab Produced TiO_2

During this project an attempt was made to create TiO_2 with Ti electrodes and a thermal plasma from an old DC welding circuit. The attempt was successful, and the resulting sample was tested in the chamber. The highest TiO_2 concentration found on the surface of this sample was 175000 ppm (a change in mass was not recorded due to the small mass). The sample was a 6" diameter concrete specimen, and the electrodes were ignited directly above the concrete specimen (0.25" to 1"). The chemistry of this reaction follows equation seen below:

$$Ti^{4+} + 2O^{2-} \rightarrow TiO_2 \quad \textbf{(85)}$$

The Ti and surrounding O_2 are ionized thus the plasma state, and the ions combine to create TiO_2 almost instantly. This beautiful reaction product can be seen in Figure [4]. The test below was performed with this product and other titanium oxides produced from the reaction[18].

Figure 30

Test of lab produced TiO_2 – 120W, 1 LPM, 1 ppm NO, RH_{avg} = 69.24%, T_{avg} = 25.68°C

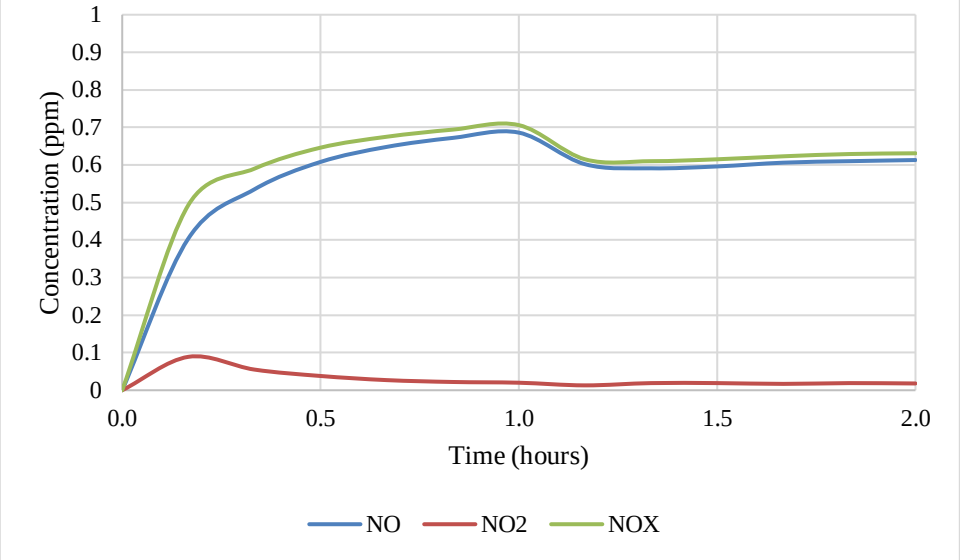

The NO_x is absorbed by the concrete specimen thus resulting in the overall lower NO_x concentration seen at the one-hour mark. The NO_x oxidation is not extremely high, but the lab produced TiO_2 is effective.

5. CONCLUSION

Conclusion of Results

The mechanics of photochemistry involved in this project were described via quantum mechanics and physical chemistry. A master curve was derived from the tests performed thus allowing the user to derive a NO_x oxidation percentage with a given TiO_2 concentration without the need to perform a test. This should allow the industry to properly choose TiO_2 concentrations for projects aimed at treated surfaces with TiO_2 for the purpose of photochemical processes. The future of this field is doping the photocatalyst of choice with a room temperature superconductor resulting in a larger total current in the semiconductor. Unfortunately, this may not happen soon thus we must find a metal and/or composite material which increases the total current in the semiconductor. Much research has been done in this area of doping the photocatalyst with a metal, but we must find an applicable material for the industry.

Future work

Again, the addition of superconducting material to the photochemical matrix will increase the photocurrent in the semiconductor interface. Such doping will also change the resonant frequency or bandgap of the material. Graphene or another superconducting material will become widely available to the public similar to salt many years ago. Humans valued salt more than gold and wars were waged over this now plentiful and cheap material. We humans will create methods for producing a superconducting material thus driving down cost and increasing availability.

REFERENCES

1. Bayar, I. (2013). Photocatalytic oxidation of NO_x over TiO_2 containing cement-based materials. *The Graduate School of Natural and Applied Sciences of Middle East Technical University*

2. Hanson, S. (2014). Evaluation of concrete containing photocatalytic titanium dioxide. *University of Utah*

3. Carp, O. (2004). Photoinduced reactivity of titanium dioxide. *Progress in Solid State Chemistry*, 32(1-2), 33-177.

4. Diebold, U. (2002). The surface science of titanium dioxide. *Surface Science Reports*, 48, 53–229.

5. Linsebigler, A. (1994). Photocatalysis on TiO_2 Surfaces: Principles, Mechanisms, and Selected Results. *Chem. Rev*., 95(3), 735-758.

6. Hassan, M. (2012). Laboratory Evaluation of Environmental Performance of Photocatalytic Titanium Dioxide Warm-Mix Asphalt Pavements. *Journal of Materials in Civil Engineering*, 24(5).

7. US EPA. (1999). Nitrogen Oxides (NO_x), Why and How They Are Controlled.

8. Dylla, H. (2011). Laboratory Investigation of the Effect of Mixed Nitrogen Dioxide and Nitrogen Oxide Gases on Titanium Dioxide Photocatalytic Efficiency in Concrete Pavements. *Journal of Materials in Civil Engineering*, 23(7).

9. Herrmann, J. (1999). Heterogeneous photocatalysis: fundamentals and applications to the removal of various types of aqueous pollutants. *Catalysis Today*, 53(1), 115–129.

10. Osborn, D. (2014). Durability Quantification of TiO_2 Surface Coating on Concrete and Asphalt Pavements. *Journal of Materials in Civil Engineering*, *26*(2).

11. Guo, R. (2017). Different Poisoning Effects of K and Mg on the Mn/TiO_2 Catalyst for Selective Catalytic Reduction of NO_x with NH_3: A Mechanistic Study. *Journal of Physical Chemistry C, 121*(14), 7881-7891.

12. Ma, J. (2014). Photocatalytic Removal of NO_x over Visible Light Responsive Oxygen-Deficient TiO_2. *The Journal of Physical Chemistry C, 118*(14), 7434-7441.

13. Wold, A. (1993). Photocatalytic Properties of TiO_2. *American Chemical Society, 5*, 280–283.

14. Kılıç, M. (2009). A Quantum Mechanical Approach to TiO_2 Photocatalysis. *Journal of Advanced Oxidation Technologies, 12*(1), 37-46.

15. Yu, Q. (2010). Indoor air purification using heterogeneous photocatalytic oxidation. Part II: Kinetic study. *Applied Catalysis B, Environmental 99*(1), 58-65.

16. Robinson, M. (2007). High resolution mapping of TiO_2 abundances on the Moon using the Hubble Space Telescope. *Geophysical Research Letters, 34*(13).

17. Narita, N. (2015). Titania may produce abiotic oxygen atmospheres on habitable exoplanets. *Scientific Reports, 5*, 13977.

18. Aliasghari, S. (2014). Plasma electrolytic oxidation of titanium. *University of Manchester, Department of Materials*.

19. Seinfeld, J. (1986). Atmospheric Chemistry and Physics of Air Pollution. *US: John Wiley & Sons, Inc.*

20. Nosaka, Y. (2016). Introduction to Photocatalysis: From Basic Science to Applications. *Cambridge, United Kingdom: The Royal Society of Chemistry*.

21. Anpo, M. (1989). Photochemistry on Solid Surfaces. *New York, US: Elsevier*

22. Pleskov, Y. (1986). Semiconductor Photoelectrochemistry. *New York, US: Consultants Bureau*.

23. Schiavello, M. (1988). Photocatalysis and Environment: Trends and Applications. *New York, US: Plenum*.

24. Kaneko, M. (2002). Photocatalysis: Science and Technology. *New York, US: Springer*.

25. Rose, A. (1963). Concepts in Photoconductivity and Allied Problems. *New York, US: Interscience Publishers*.

26. Japanese Industrial Standard. (2016). Fine ceramics (advanced ceramics, advanced technical ceramics)-Test method for air purification performance of photocatalytic materials-Part 1: Removal of nitric oxide. *Tokyo, Japan: Japanese Standards Association*.

27. Hanlon, T. (2023, February 22). The Band Theory of Solids. Retrieved from https://www.pathwayz.org/Tree/Plain/BAND+THEORY

28. Giannakopoulou, T. (2012). Composite hydroxyapatite/TiO2 materials for photocatalytic oxidation of NOx. *Materials Science and Engineering B*, 177(13), 1046-1052.

29. Hu, Y., Song, X., Jiang, S., & Wei, C. (2015). Enhanced photocatalytic activity of Pt-doped TiO2 for NOx oxidation both under UV and visible light irradiation: A synergistic effect of lattice Pt4+ and surface PtO. *Chemical Engineering Journal*, *274*, 102-112.

30. Todorova, N., Vaimakis, T., Petrakis, D., Hishita, S., Boukos, N., Giannakopoulou, T., ... & Trapalis, C. (2013). N and N, S-doped TiO2 photocatalysts and their activity in NOx oxidation. *Catalysis today*, *209*, 41-46.

31. Trapalis, A., Todorova, N., Giannakopoulou, T., Boukos, N., Speliotis, T., Dimotikali, D., & Yu, J. (2016). TiO2/graphene composite photocatalysts for NOx

removal: A comparison of surfactant-stabilized graphene and reduced graphene oxide. *Applied Catalysis B: Environmental*, *180*, 637-647.

32. Martinez-Oviedo, A., Ray, S. K., Nguyen, H. P., & Lee, S. W. (2019). Efficient photo-oxidation of NOx by Sn doped blue TiO2 nanoparticles. *Journal of Photochemistry and Photobiology A: Chemistry*, *370*, 18-25.

33. Papailias, I., Todorova, N., Giannakopoulou, T., Yu, J., Dimotikali, D., & Trapalis, C. (2017). Photocatalytic activity of modified g-C3N4/TiO2 nanocomposites for NOx removal. *Catalysis Today*, *280*, 37-44.

34. Maggos, T., Bartzis, J. G., Liakou, M., & Gobin, C. (2007). Photocatalytic degradation of NOx gases using TiO2-containing paint: A real scale study. *Journal of hazardous materials*, *146*(3), 668-673.

35. Ishibai, Y., Sato, J., Akita, S., Nishikawa, T., & Miyagishi, S. (2007). Photocatalytic oxidation of NOx by Pt-modified TiO2 under visible light irradiation. *Journal of Photochemistry and Photobiology A: Chemistry*, *188*(1), 106-111.

36. Wang, H., Wu, Z., Zhao, W., & Guan, B. (2007). Photocatalytic oxidation of nitrogen oxides using TiO2 loading on woven glass fabric. *Chemosphere*, *66*(1), 185-190.

37. Rodríguez, M. H., Melián, E. P., Díaz, O. G., Araña, J., Macías, M., Orive, A. G., & Rodríguez, J. D. (2016). Comparison of supported TiO2 catalysts in the photocatalytic degradation of NO_x. *Journal of Molecular Catalysis A: Chemical*, *413*, 56-66.

38. Ye, B., Lee, M., Jeong, B., Kim, J., Lee, D. H., Baik, J. M., & Kim, H. D. (2019). Partially reduced graphene oxide as a support of Mn-Ce/TiO_2 catalyst for selective catalytic reduction of NO_x with NH_3. *Catalysis Today*, *328*, 300-306.

39. Wu, G., Feng, X., Zhang, H., Zhang, Y., Wang, J., Chen, Y., & Dan, Y. (2018). The promotional role of Ni in $FeVO_4/TiO_2$ monolith catalyst for selective catalytic reduction of NO_x with NH_3. *Applied Surface Science*, *427*, 24-36.

40. Dalton, J. S., Janes, P. A., Jones, N. G., Nicholson, J. A., Hallam, K. R., & Allen, G. C. (2002). Photocatalytic oxidation of NO_x gases using TiO_2: a surface spectroscopic approach. *Environmental Pollution*, *120*(2), 415-422.

41. *The 5 Methods of Air Purification*. (n.d.). Elemental Air Systems. Retrieved March 7, 2023, from https://elementalairsystems.com/blogs/air-education-blog/the-5-methods-of-air-purification

42. *Filtration media*. (n.d.). Www.lenntech.com. Retrieved March 7, 2023, from https://www.lenntech.com/products/filtration-media/filtration-media.htm

43. Murray, L. T. (2016). Lightning NO_x and impacts on air quality. *Current Pollution Reports*, *2*, 115-133.

44. Ahmad, A., Dempsey, S. K., Daneva, Z., Azam, M., Li, N., Li, P. L., & Ritter, J. K. (2018). Role of nitric oxide in the cardiovascular and renal systems. *International journal of molecular sciences*, *19*(9), 2605.

45. Jarvis, D. J., Adamkiewicz, G., Heroux, M. E., Rapp, R., & Kelly, F. J. (2010). Nitrogen dioxide. *WHO guidelines for indoor air quality: Selected pollutants*. World Health Organization.

46. Noll, K. E., & Crowder, J. W. (1992). Control of Gases and Vapors by Adsorption, Absorption and Condensation. In *Industrial Air Pollution: Assessment and Control* (pp. 145-154). Springer Berlin Heidelberg.

47. Aditya, R. (2018). A review of general and modern methods of air purification. *Journal of Thermal Engineering*, *5*(2), 22-28.

48. Oil and Colour Chemists' Association, Australia, & Oil and Colour Chemists' Association, Australia. (1983). Titanium Dioxide Pigments. *Surface Coatings: Vol I-Raw Materials and Their Usage*, 305-312.

49. *Wikipedia Contributors*. (2019, October 5). Titanium dioxide. Wikipedia; Wikimedia Foundation. https://en.wikipedia.org/wiki/Titanium_dioxide

APPENDIX A

Figure 31

E2 - 50W, 1 LPM, 1 ppm NO, no RH and temperature data, no water in chamber

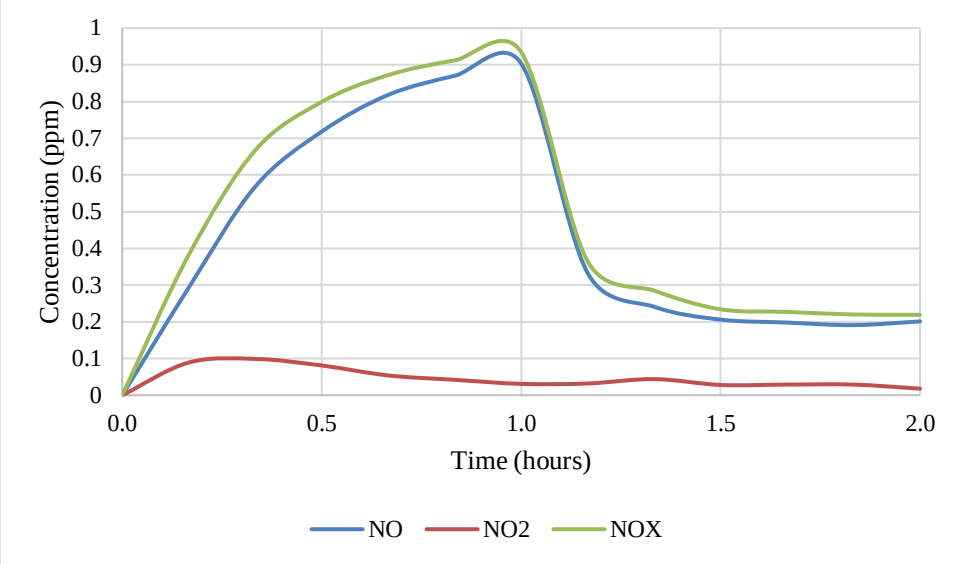

Figure 32

E3 – 50W, 1 LPM, 1 ppm NO, no RH and temperature data

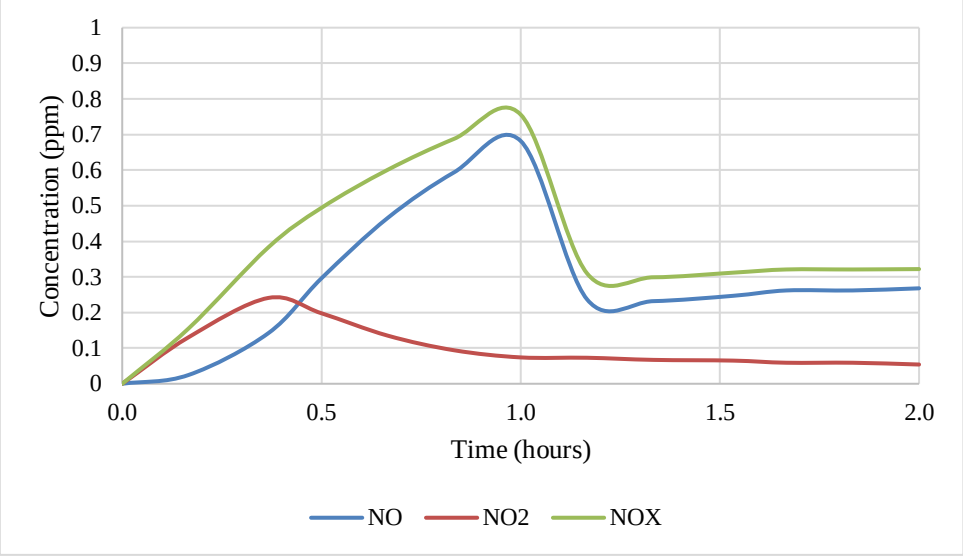

Figure 33

F2 – 120W, 1 LPM, 2 ppm NO, RH_{avg} = 67.25%, T_{avg} = 25.31°C

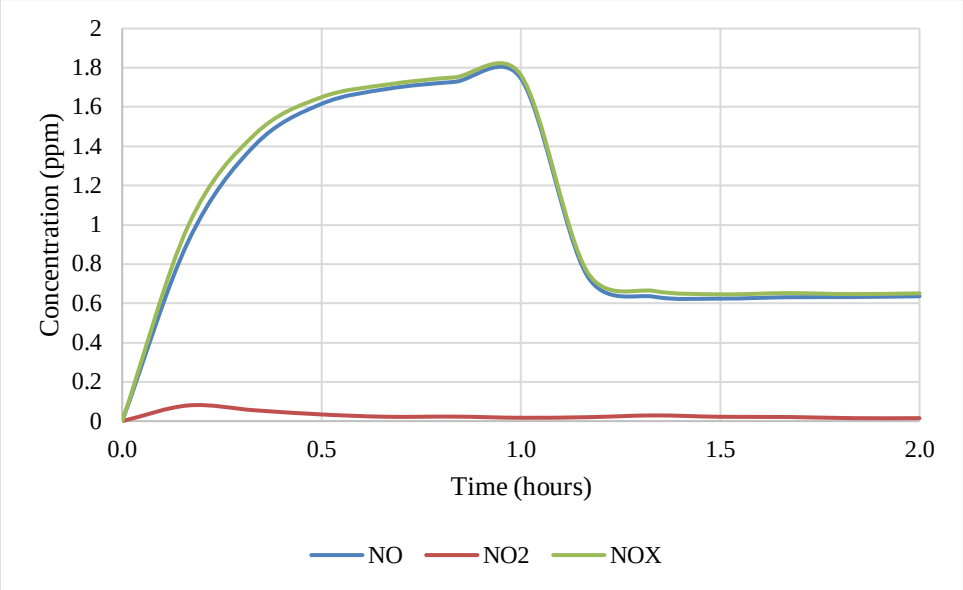

Figure 34

F2 – 120W, 1 LPM, 5 ppm NO, RH_{avg} = 69.06%, T_{avg} = 24.60°C

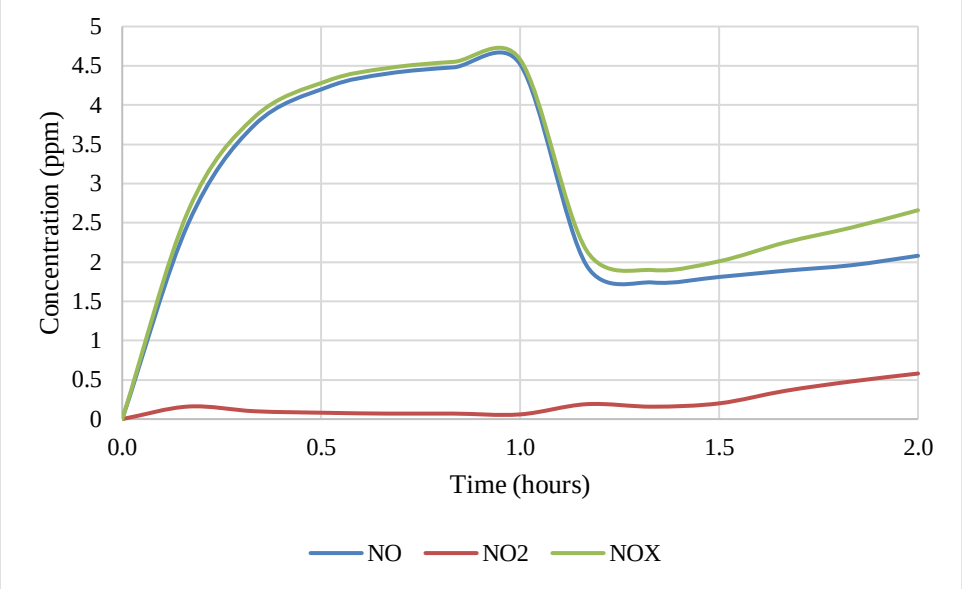

Figure 35

F2 – 120W, 1 LPM, 10 ppm NO, RH_{avg} = 68.65%, T_{avg} = 26.63°C

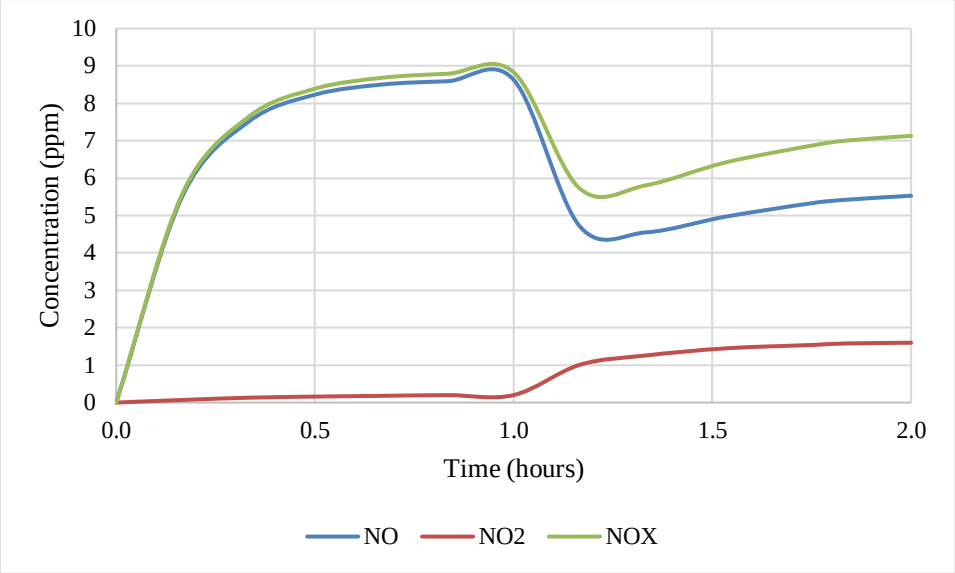

Figure 36

F3 – 120W, 1 LPM, 2 ppm NO, RH_{avg} = 72.32%, T_{avg} = 25.81°C

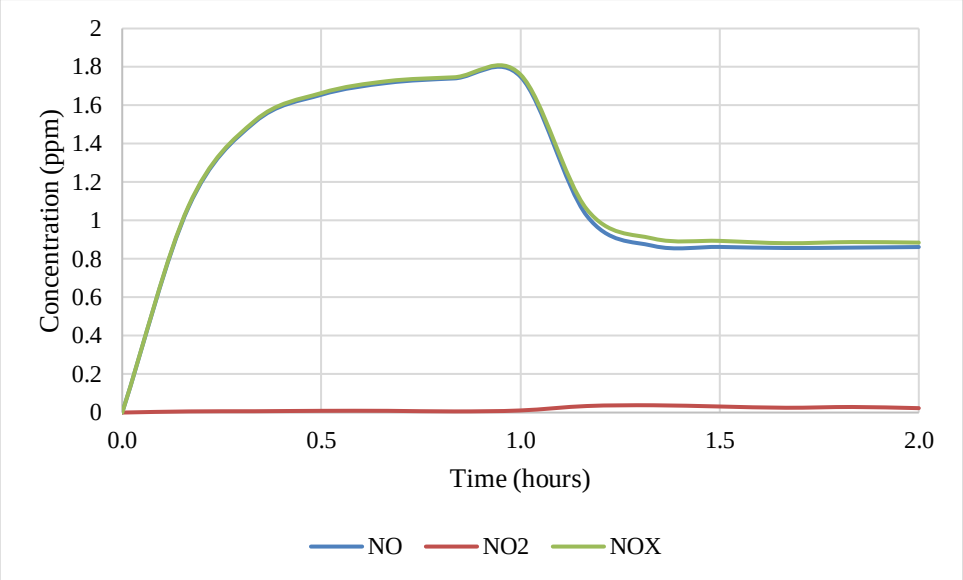

Figure 37

F3 – 120W, 1 LPM, 5 ppm NO, RH_{avg} = 71.59%, T_{avg} = 24.53°C

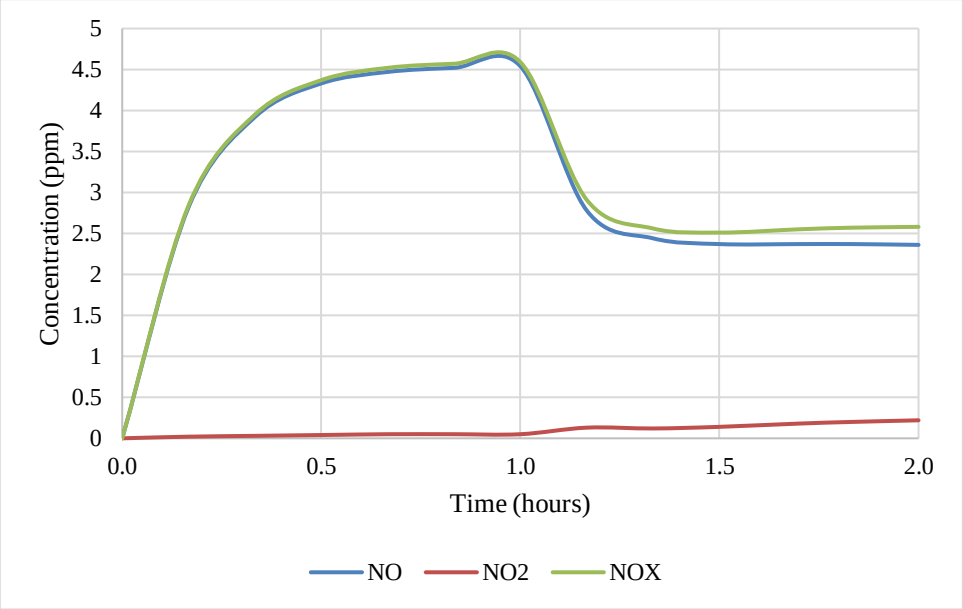

Figure 38

F3 – 120W, 1 LPM, 10 ppm NO, RH_{avg} = 65.68%, T_{avg} = 25.63°C

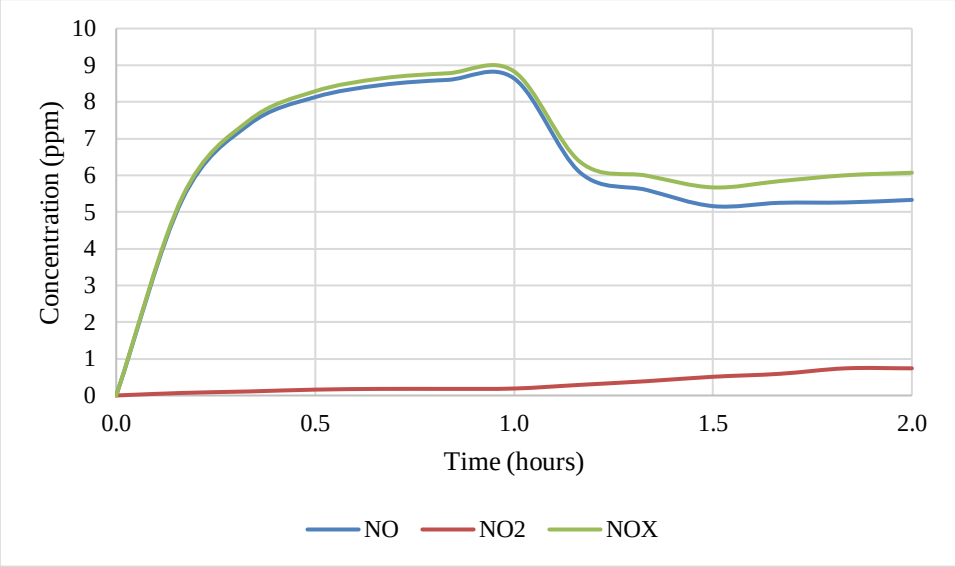

Figure 39

H2 – 120W, 1 LPM, 1 ppm NO, RH_{avg} = 70.91%, T_{avg} = 28.15°C

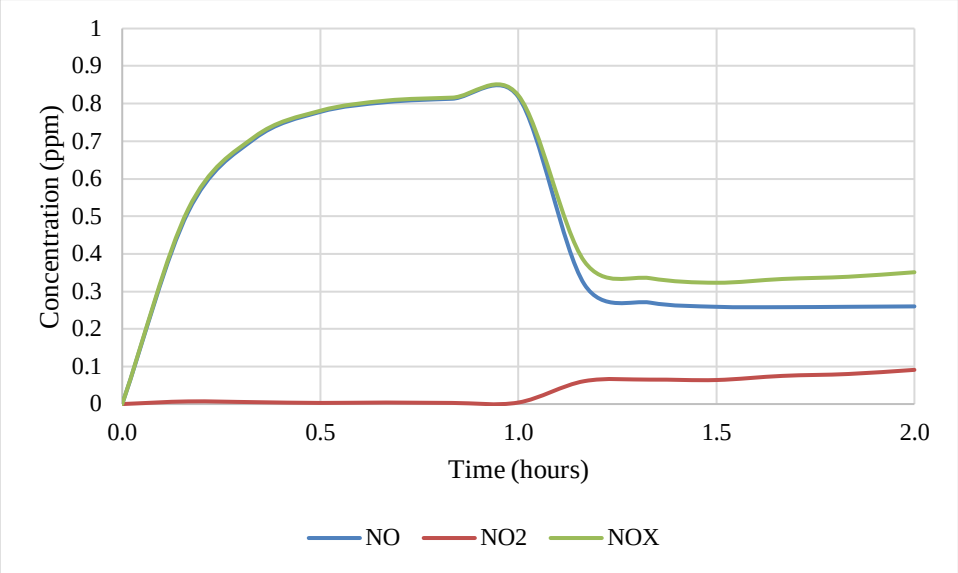

Figure 40

H3 – 120W, 1 LPM, 1 ppm NO, RH_{avg} = 71.28%, T_{avg} = 28.17°C

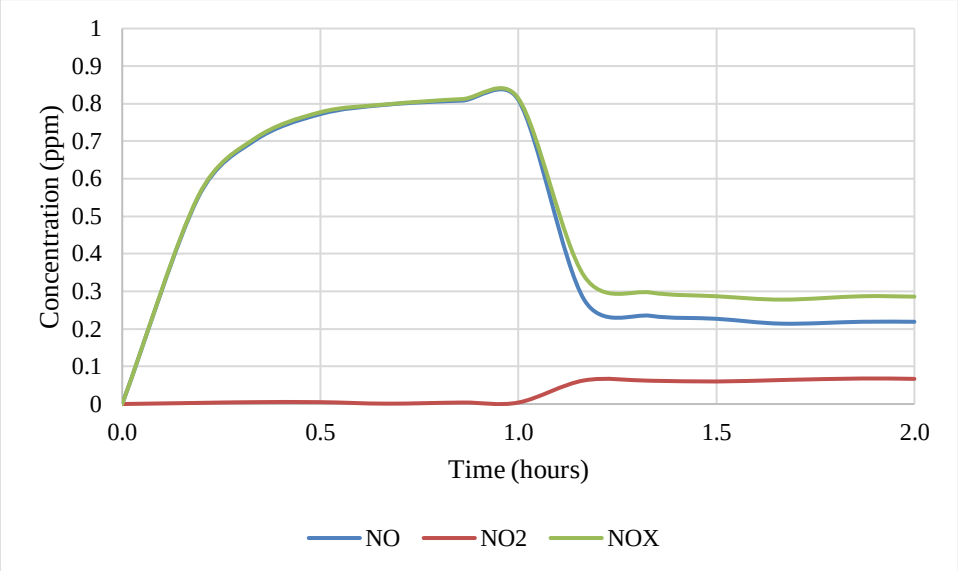

Figure 41

H5 – 120W, 1 LPM, 1 ppm NO, RH_{avg} = 69.53%, T_{avg} = 27.35°C

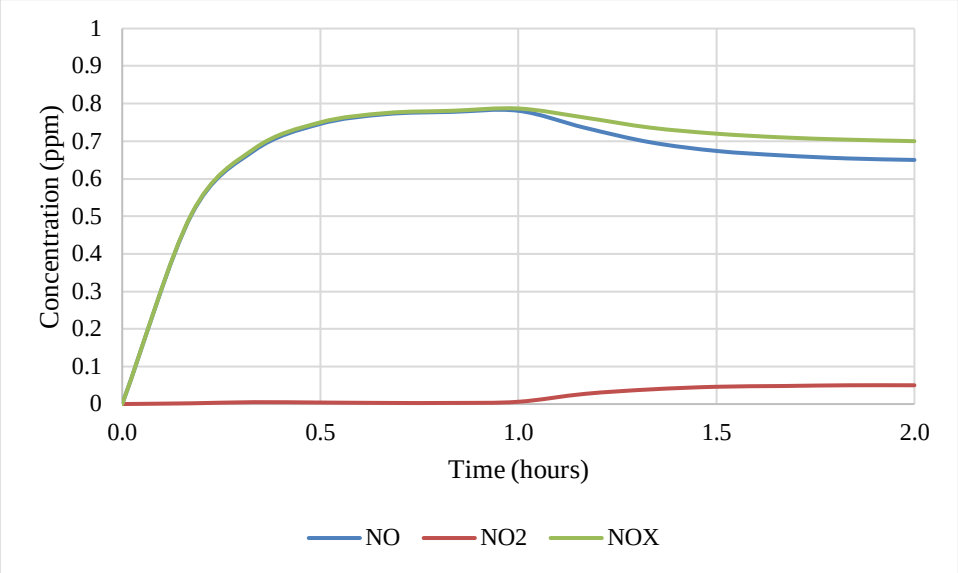

Figure 42

H6 – 120W, 1 LPM, 1 ppm NO, RH_{avg} = 75.62%, T_{avg} = 27.40°C

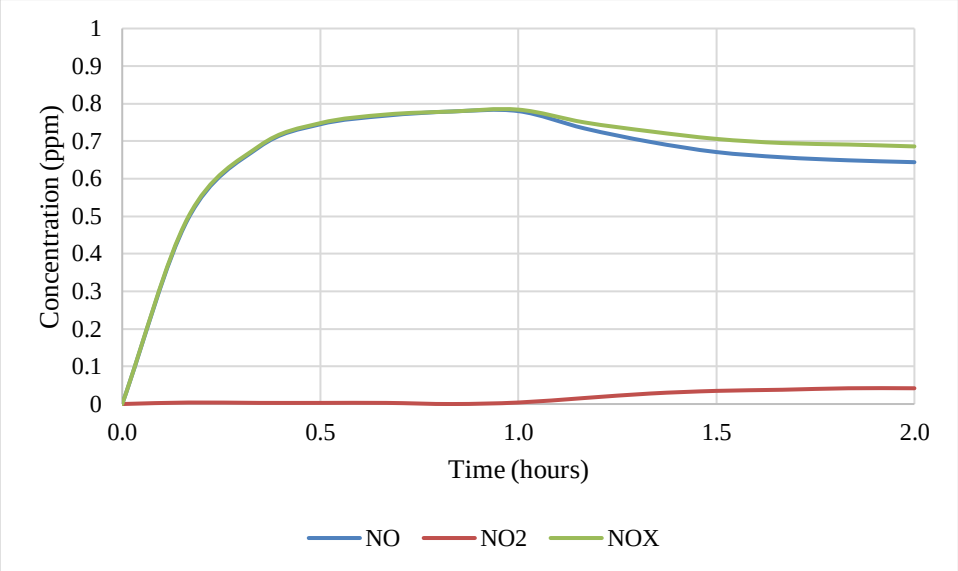

Figure 43

C1 – 120W, 1 LPM, 1 ppm NO, no RH and temperature data (no water in chamber)

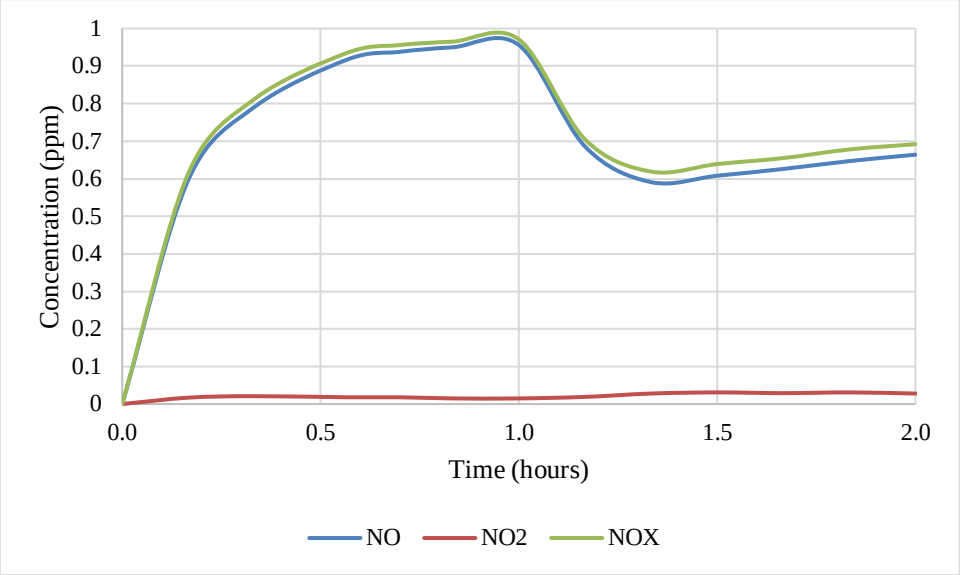

Figure 44

Chamber with Arduino and DHT-11 sensor

Figure 45

375nm LED (max power ~120W)

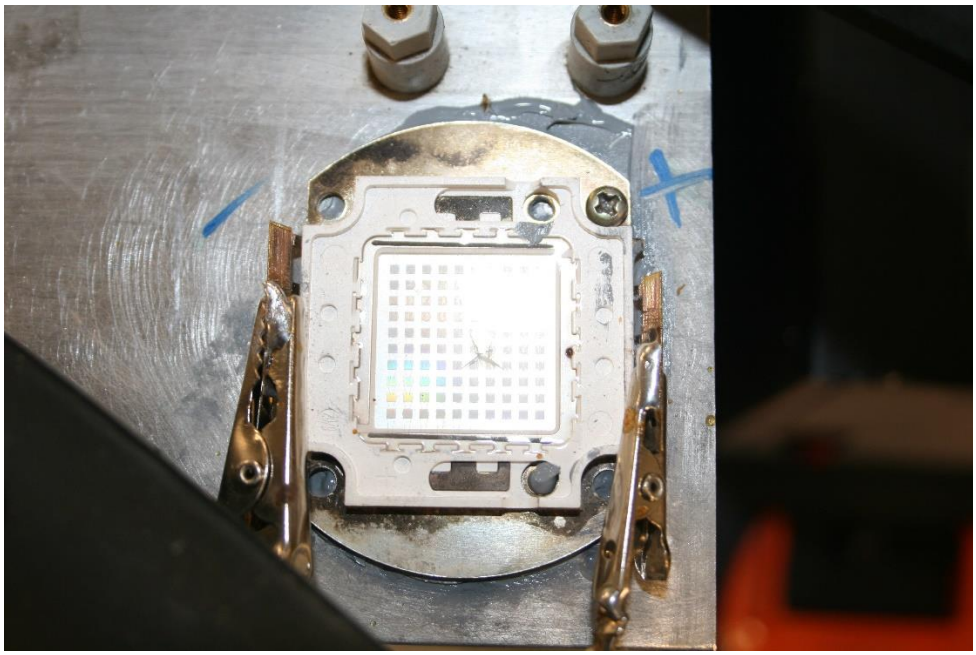

Figure 46

Analog Regulator in first 3-way valve

Figure 47

110 ppm nitric oxide (NO) blended with air

Figure 48

Zero grade air

Figure 49

Nitrogen

Figure 50

Set E – E1, E2 and E3 from right to left

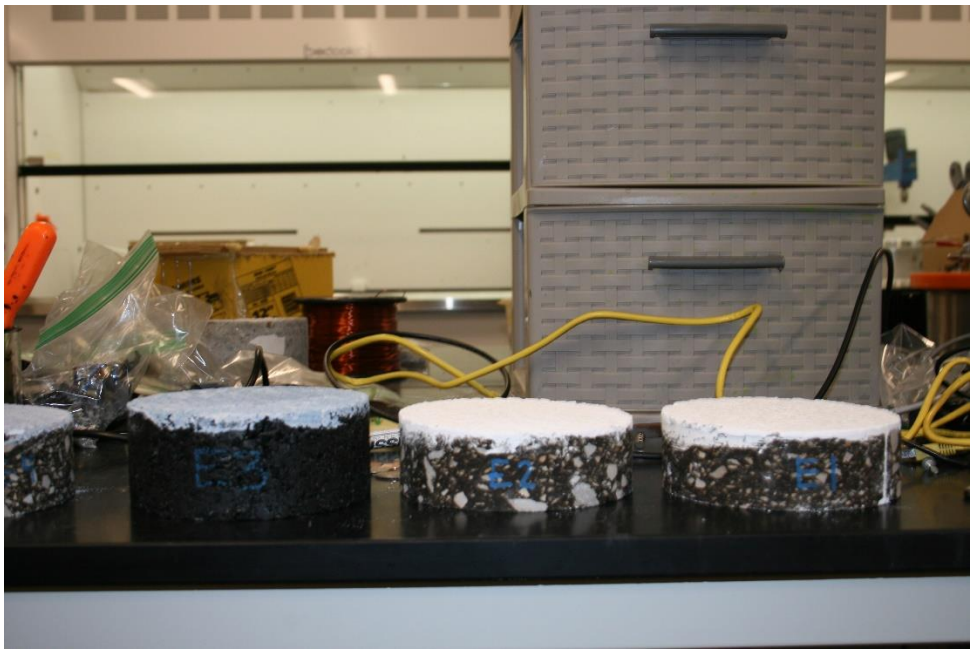

Figure 51

Set F – F1

Figure 52

Set F – F2

Figure 53

Set F – F3

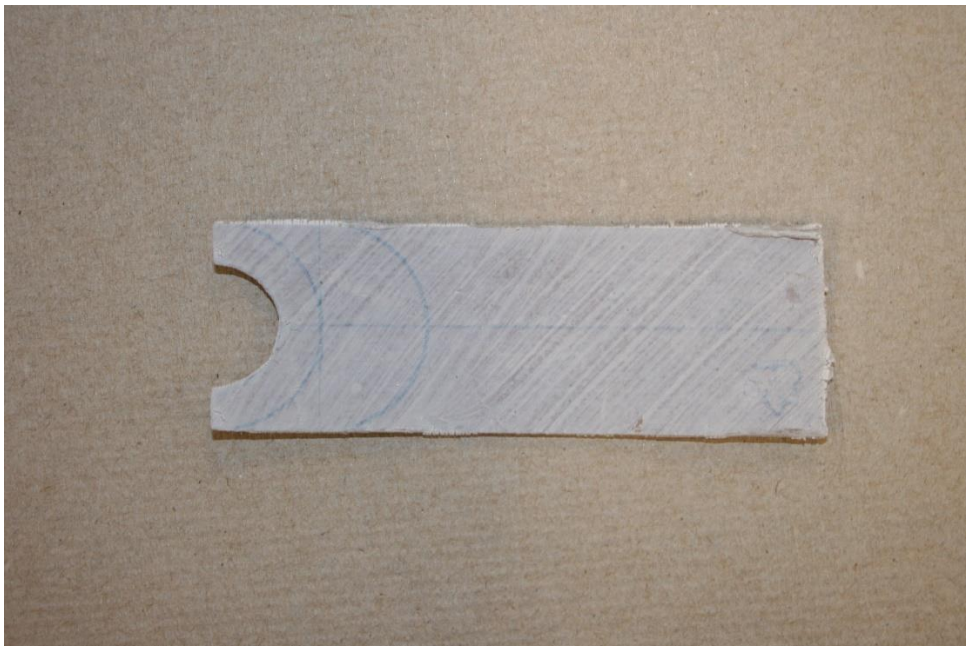

Figure 54

Set H – H1, H2 and H3 from left to right

Figure 55

Set H – H4, H5 and H6 from left to right

Figure 56

Charlotte, NC 9156.2

Figure 57

Charlotte, NC 8672.2

Figure 58

Sample tested with lab produced TiO_2 deposits

Figure 59

Circuit elements used to create TiO_2

APPENDIX B

SOME PHYSICS OF THE IRRADIADED SEMICONDUCTOR AND NO_X CHEMISTRY

Introduction[1-4]

Photocatalysis is an electrical or quantum mechanical phenomenon. For a photochemical reaction to occur a current known as the photocurrent must be induced by an accelerated charge or electromagnetic radiation. Each semiconductor has a certain resonant frequency wherein the photocatalytic performance for said semiconductor is at a maximum. This frequency is determined by the bandgap of the semiconductor, and the bandgap is equivalent to wavelength thus providing a resonant frequency for a specific bandgap. TiO_2 has a bandgap of ~3.2 eV, and this number varies as metals are doped onto the TiO_2. This so-called bandgap is the energy difference between the top of the valence band and the bottom of the conductance band. The valence band has the highest concentration of electrons, and the conduction band has the lowest concentration of electrons. The action of this phenomenon is very similar to a diode where an alternating current is applied to the diode and the current is rectified by the diode. The semiconductor medium rectifies the high frequency current (UV radiation for example) and generates an electric field known as the space charge. It is the pure geometry of the TiO_2 lattice and the dipoles within which act as a full bridge rectifier and provide a means for generating a uniform electric field gradient. Increasing surface area or decreasing particle size will result in higher total currents. Doping TiO_2 with various metals such as Li, Na, K, Cs, Ca, Mg, Al, Si, V, Nb, Cr, Mo, Mn, Fe, W, Co, Rh, Ir, Ni, Pd, Pt, Cu, Ag, Ag, and Sn provide

higher total currents with respect to pure TiO_2 (doping does not always mean a higher total current but the Schottky diode created by the added metal generally creates a higher total current than the pure semiconductor). The ultimate solution for highly efficient photocatalysts is extremely high total currents. This can be achieved by adding a superconducting material to the matrix of the photocatalyst. Thus, a superconducting derivation of TiO_2 or some other photocatalyst will be the future of this field. For now, the focus is on pure TiO_2 which has yet to be used widely in the construction industry, and a super material will have an even smaller chance of implementation.

Electromagnetic Waves and Optical Properties of Solids[20]

This type of chemistry is dependent on quantum chemistry; in other words, the behavior of the semiconductor is dependent on where the electrons are in the atom. This requires an analysis using classical electrodynamics (Maxwell-Heaviside's equations). Below is the equation for the electric field or energy, E:

$$\mathrm{E} = \frac{1240}{\lambda} \qquad \textbf{(1)}$$

In equation **(1),** E is energy in eV and λ is wavelength in nm; with 3.2 eV as the input for E from the bandgap number of TiO_2 we obtain 387.5 nm or 773.7 THz. This is the frequency of electromagnetic radiation at which the maximum photocurrent can be achieved in the TiO_2. 1240 in equation **(1)** is calculated from $\mathrm{ch}/(\mathrm{e}10^{-9})$. The energy in equation **(1)** can be calculated by Maxwell-Heaviside's equations via the electric and magnetic field interaction with a material of electrical conductivity σ.

$$\mathrm{D} = \varepsilon\mathrm{E} = \varepsilon_0\varepsilon_1\mathrm{E} \qquad \textbf{(2)}$$

$$B = \mu H = \mu_0 \mu_1 H \quad \textbf{(3)}$$

When electromagnetic radiation imparts its momentum on an object said objects electrons experience an electric field (E) and a magnetic field (H). D is the electric flux density and B is the magnetic flux density. A differential equation can be formed using vector or tensor analysis which can describe the electric field in one direction.

$$\nabla^2 E - \sigma\mu_0 \frac{\partial E}{\partial t} - \varepsilon_0 \varepsilon_1 \mu_0 \frac{\partial^2 E}{\partial t^2} = 0 \quad \textbf{(4)}$$

The solution to this equation is given below

$$E_x = E_0 e^{-i\omega(t-\frac{z}{v})} \quad \textbf{(5)}$$

and the velocity of this wave is given by

$$\frac{1}{v} = \sqrt{\mu_0(\varepsilon_0\varepsilon_1 + i\frac{\sigma}{\omega})} \quad \textbf{(6)}$$

If the complex permittivity is described as $\varepsilon^* = \varepsilon_1 + i\varepsilon_2$ then equation **(6)** becomes

$$\frac{1}{v} = \sqrt{\mu_0 \varepsilon_0 \varepsilon^*} \quad \textbf{(7)}$$

with $\varepsilon_2 = \sigma/\omega\varepsilon_0$. The complex refractive index must be described as $n^* = n + ik$ which will allow the user to relate the velocity of the electromagnetic wave to the refractive nature of the material. In other words, the velocity of the electromagnetic wave of said material is dependent on the complex permittivity and refractive index which are one in the same.

$$\frac{1}{v} = \frac{n^*}{c} = \frac{n + ik}{c} \quad \textbf{(8)}$$

If we substitute this back into equation **(5)** we will obtain the following relationship.

$$E_x = E_0 e^{-i\omega\left(t-\frac{nz}{c}\right)} e^{-\left(\frac{\omega k}{c}\right)z} \quad \textbf{(9)}$$

The oscillation of the electric field along the x-axis is dependent on time, the refractive index, the distance along the z-axis, the angular frequency, and the imaginary part of the refractive index. Given all these parameters we can describe the real and complex parts of the permittivity and refractive index.

$$\varepsilon_1 = n^2 - k^2 \quad \textbf{(10)}$$

$$\varepsilon_2 = 2nk = \frac{\sigma}{\omega\varepsilon_0} \quad \textbf{(11)}$$

$$n = \sqrt{0.5\left(\sqrt{\varepsilon_1^2 + \varepsilon_2^2} + \varepsilon_1\right)} \quad \textbf{(12)}$$

$$k = \sqrt{0.5\left(\sqrt{\varepsilon_1^2 + \varepsilon_2^2} - \varepsilon_1\right)} \quad \textbf{(13)}$$

This unique set of equations allows the user to extract n and k with the complex permittivity and visa-versa. Given this conclusion we can now describe the absorption coefficient α in terms of the material's electrical conductivity σ or ε_2 as seen below.

$$\alpha = \frac{\sigma}{c\varepsilon_0 n} = \frac{\omega\varepsilon_2}{cn} = \frac{2\omega k}{c} \quad \textbf{(14)}$$

Now we reapproach the complex permittivity with the Drude model:

$$\varepsilon^*(\omega) = 1 - \frac{\omega_p^2}{\omega\left(\omega + \frac{i}{\tau}\right)} \quad \textbf{(15)}$$

$$\omega_p = \sqrt{\frac{e^2 N_0}{\varepsilon_0 m^*}} \tag{16}$$

where τ is the lifetime of the free carrier and N_0 is the carrier density. Now the absorption coefficient can be described by the wavelength.

$$\alpha = \frac{\omega \varepsilon_2}{cn} = \frac{e^3 \lambda^2 N_0}{4\pi^2 c^3 \varepsilon_0 m^{*2} n \mu} \tag{17}$$

From the equation above we can conclude the free carrier absorption increases with an increase in wavelength. It must be noted the intensity I of the electromagnetic wave is proportional to the square of the amplitude of the electric field.

$$I = |E_x|^2 \propto e^{-\alpha z} \tag{18}$$

Semiconductors and Quantum Chemistry[14,21-25,27]

The dispersion law or energy of a particle of semiconductor material for a given wave number k can be described as such:

$$E(k) = \pm \frac{\hbar^2 k^2}{2m^*} \tag{19}$$

where m^* is generally expressed as a relative value with respect to the electron mass. Here $\hbar k$ represents the momentum p of the particle which is obtained by the de Broglie equation $p = h/\lambda$ with $k = 2\pi/\lambda$. With the proper input the energy of the semiconductor can be established thus giving us the bandgap energy. First view Figure [60] to understand how the bandgap can describe a solid. The energy levels of the upper edge of

the valence band $E_v(k)$ and the bottom edge of the conduction band $E_c(k)$ can be described as follows with the wave number k:

$$E_v(k) = -\frac{\hbar^2 k^2}{2m_v} \tag{20}$$

$$E_c(k) = E_g + \frac{\hbar^2 k^2}{2m_c} \tag{21}$$

If a material is an insulator or semiconductor the Fermi energy E_F will fall in between the top of the valence band and the bottom of the conduction band. For a metal the Fermi energy falls onto one of the bands thus connecting the bands, hence the Fermi Sea of electrons. The Fermi energy can be described as the energy level below energy level the electrons occupy but above the energy level where the electrons are vacant. The Fermi energy is naturally dissipated via thermodynamic losses given by $k_B T$ where k_B is the Boltzmann constant. First, we must start with the Fermi level which is the thermodynamic work required to add one electron to the system. For an intrinsic semiconductor the Fermi level can be described as such:

$$F = E_c - 0.5E_g - 0.5k_B T \ln\frac{N_c}{N_v} \tag{22}$$

The Fermi levels for p-type and n-type semiconductors are respectively as follows:

$$F = E_v + k_B T \ln\frac{N_v}{N_A} \tag{23}$$

$$F = E_c - k_B T \ln\frac{N_c}{N_D} \tag{24}$$

For the p-type semiconductor $N_A \cong p_0$ and for the n-type semiconductor $N_D \cong n_0$. The Fermi level is a descriptor of degeneracy for a given solid. An example of a degenerate

solid is a conducting metal or a doped semiconductor. Insulators and semiconductors are non-degenerate solids. One can conclude that a conductive solid is degenerate, and a non-conductive solid is non-degenerate. Non-degeneracy is more clearly defined by the following inequality:

$$E_v + 3k_BT \leq F \leq E_c - 3k_BT \quad \textbf{(25)}$$

A degenerate semiconductor must be within $3k_BT$ of one of the band edges; the n-type will approach E_c and p-type will approach E_v. A degenerate semiconductor can also have a Fermi level which falls onto a band; all conductive metals have this characteristic. Thus, the non-degenerate semiconductor has a Fermi level which falls well within the bandgap following the above inequality. Photoexcitation of a semiconductor can be described has the shift of the Fermi level causing non-degenerate semiconductor to become a degenerate semiconductor. Following this the Fermi energy must be addressed. The Fermi energy is described by the equilibrium concentration of electrons in the bulk and the effective mass of an electron in the conduction band

$$E_F = \frac{(3\pi^2)^{\frac{2}{3}}\hbar^2 n_0^{\frac{3}{2}}}{2m_c} \quad \textbf{(26)}$$

and the equilibrium concentration of electrons and holes in the semiconductor bulk can be seen below.

$$n_0 = N_c \exp\left(\frac{F - E_c}{k_BT}\right) \quad \textbf{(27)}$$

$$p_0 = N_v \exp\left(\frac{E_v - F}{k_BT}\right) \quad \textbf{(28)}$$

where

$$N_{c,v} = 2.5 \times 10^{19}(\frac{m_{c,v}}{m_0})^{1.5}(\frac{T}{300})^{1.5}\ cm^{-3} \quad \textbf{(29)}$$

Notice the equilibrium concentration of electrons and holes in the bulk is directly related to the number of quantum states in the respective band. This number of states is then multiplied by the exponential of the difference between the respective band and the Fermi level or electrochemical potential. Thus, the location of the Fermi level or the degeneracy of the semiconductor is directly related to the concentration of charge carriers in the bulk. Given the insight of the Fermi level it is a good time to introduce the thermodynamic electronic work function denoted as w_T. The work function is the difference between the potential energy of an electron just outside the surface forces (E_{vac}) and the Fermi level or electrochemical potential. This can be described in the equation below as[5]:

$$w_T = E_{vac} - F \quad \textbf{(30)}$$

The work function can be described as the minimum amount of energy needed to remove an electron of maximum energy from the semiconductor bulk. As seen above the degeneracy of the semiconductor is directly related to the work function. The thermoemission saturation current density of a solid can be used to determine the work function as follows:

$$I_T = AT^2 \exp\left(-\frac{w_T}{k_B T}\right) \quad \textbf{(31)}$$

where

$$A \equiv \frac{4\pi e k_B^2 m_0}{(2\pi\hbar)^3} \quad \textbf{(32)}$$

The work function is a descriptor of the semiconductor properties like the bandgap energy. It ultimately tells us how electrons are emitted from the bulk or solid. The change in the work function shows the semiconductor reacts to a given quantum flux and can be described as such:

$$\Delta w_T = -e\phi_{SC} \quad \textbf{(33)}$$

Thus the change in the work function is equivalent to the unit charge dotted with the voltage of the space charge layer. The change in thermodynamic work or temperature is directly related to the charge and thus the capacitance of the semiconductor. This leads us to the probability of states in the semiconductor bulk. The probability of the state with energy E being occupied by an electron is given by the Fermi-Dirac function:

$$f(E,T) = (1 + e^{(\frac{E-F}{k_B T})})^{-1} \quad \textbf{(34)}$$

These electrons must be quasi-particles with half-integral spin. With this function the concentrations of charge carriers can be calculated.

The Space Charge Layer[20]

To calculate the space charge layer the Poisson-Boltzmann equation must be employed:

$$\frac{d^2\phi(x)}{dx^2} = -\frac{\rho}{\varepsilon_0 \varepsilon} \quad \textbf{(35)}$$

It can be approximated that $\rho = eN_0$. The former equation can be solved if $\frac{d\phi(x)}{dx} = 0$ and $\phi(x) = 0$ at $x = L_{SC}$.

$$\phi(x) = -\frac{eN_0}{2\varepsilon_0\varepsilon}(x - L_{SC})^2 \quad \textbf{(36)}$$

If $\phi_{SC} = -\phi(0)$ the thickness of the space charge layer can be found.

$$L_{SC} = \sqrt{\frac{2\varepsilon_0\varepsilon\phi_{SC}}{eN_0}} \quad \textbf{(37)}$$

The space charge layer can also be defined by the external potential U and the flat band potential U_{fb}. The flat band potential is the potential at the depletion layer where the space charge region terminates. Thus, the space charge layer can be redefined in terms of energy:

$$\phi_{SC} = U - U_{fb} - \frac{k_B T}{e} \quad \textbf{(38)}$$

The electric charge within the space charge layer can be described as:

$$Q_{SC} = eN_0 L_{SC} = \sqrt{2\varepsilon_0\varepsilon eN_0(U - U_{fb} - \frac{k_B T}{e})} \quad \textbf{(39)}$$

With the charge of the space charge layer, we can find the differential capacitance which can be experimentally determined with an impedance meter:

$$C_{SC} = \frac{dQ_{SC}}{dU} \quad \textbf{(40)}$$

With this capacitance the Mott-Schottky plot can be determined which allows the user to find N_0 and U_{fb} experimentally. Now the Poisson-Boltzmann equation is to be resolved for a particle of radius a

$$\frac{1}{r^2}\frac{\partial}{\partial r}(r^2\frac{\partial\phi}{\partial r}) = \frac{eN_0}{\varepsilon_0\varepsilon} \quad \textbf{(41)}$$

and under the condition of $\frac{d\phi}{dr} = 0$ at $r = a - L_{SC}$ the solution is:

$$\phi(r) = \frac{eN_0}{6\varepsilon_0\varepsilon}(r - a + L_{SC})^2\left(1 + \frac{2(a - L_{SC})}{r}\right) \quad \textbf{(42)}$$

Particle size is an extremely important factor in photocatalytic performance. This ultimately reduces to the quantum yield or electric potential for a given volume of TiO_2. This can also be seen in equation **(43)**:

$$\phi = \frac{\int \sum_n \sum_m nk_e X_m^n dt}{\int g(t) V dt} \quad \textbf{(43)}$$

Thus, if the volume of the TiO_2 particle is small the quantum yield will be high for that given volume of TiO_2. This high quantum yield is in direct proportion to the surface area of the TiO_2.

Moving Charges in a Degenerate Semiconductor[20,21-25]

The resulting chemical reaction at hand which is produced say by an irradiated (375 nm) piece of TiO_2 is entirely dependent on the work done by the induced charge carriers in the semiconductor (TiO_2). For these charge carriers to exert work onto the lattice they must move a finite distance, thus the moving charge. This results in a current in the semiconductor bulk which generates a voltage. This voltage and current are the reason we have a photochemical reaction. With these facts the photocurrent is introduced which can be described as the difference between the current in the semiconductor with and without irradiation.

$$i_{ph} = i_{light} - i_{dark} \quad \textbf{(44)}$$

An example from one of the references will give an idea of how a p-type semiconductor with only a hole current can be evaluated. Thus, we start with a photocurrent which is only comprised of a hole current:

$$i_{ph} = i_{dl} - i_b \tag{45}$$

where i_{dl} is the current determined by the generation of holes in the depletion layer and i_b is the hole current in the semiconductor bulk. Using the following equations

$$g(x) = \alpha_L(\omega) J_0 e^{-\alpha_L x} \tag{46}$$

$$\int_0^\infty g(x)dx = J_0 \int_0^\infty \alpha_L e^{-\alpha_L x} dx = J_0 \tag{47}$$

where $\alpha_L = 2\alpha\omega/c$. The following are used to calculate the current of holes in the semiconductor bulk. Below is the current in the depletion layer:

$$i_{dl} = -e \int_0^{L_{SC}} g(x)dx = eJ_0(e^{-\alpha_L L_{SC}} - 1) \tag{48}$$

For the quasi-neutral bulk, the following equation is obtained

$$D_p \frac{d^2 p}{dx^2} - \frac{p - p_0}{\tau_p} + \alpha_L J_0 e^{-\alpha_L x} = 0 \tag{49}$$

and yields the following result:

$$p(x) = p_0 - (p_0 + Ae^{-\alpha_L L_{SC}}) e^{\frac{L_{SC} - x}{L_p}} + Ae^{-\alpha_L x}$$

where

$$A \equiv \frac{J_0 \alpha_L}{D_p(\alpha_L^2 - L_p^{-2})}$$

Now the diffusion current of holes can be determined.

$$i_b = -eJ_0 \frac{\alpha_L L_p}{1 + \alpha_L L_p} e^{-\alpha_L L_{SC}} \quad \textbf{(50)}$$

With the two currents i_{dl} and i_b the photocurrent can be calculated as

$$i_{ph} = eJ_0\left(1 - \frac{e^{-\alpha_L L_{SC}}}{1 + \alpha_L L_p}\right) \quad \textbf{(51)}$$

This photocurrent is only for the semiconductor used in this problem which is assumed to only produce a positive current of holes. In experimentation the electron and hole currents will both be present, and the magnitude of such currents is dependent on the semiconductor type, degeneration, and doping. The following equations can be used generally with the approach of the semiconductor in contact with an electrolyte surface:

$$i_n = \frac{eD_n}{Z}(N_D - n_s e^{-Y}) \quad \textbf{(52)}$$

$$i_p = \frac{eD_p}{L_p}(p_s e^{Y} - p_0) + eJ_0\left(\frac{e^{-\alpha_L L_{SC}}}{1 + \alpha_L L_p} - 1\right) \quad \textbf{(53)}$$

where

$$Z = L_D\sqrt{2}\int_0^{|Y|^{0.5}} e^{t^2} dt$$

$$Y = \frac{e\phi_{SC}}{k_B T}$$

The current in the semiconductor can be calculated following the procedure in the first example.

Oxidation Chemistry of Adsorbed NO_x onto TiO_2[15]

All the constituents of the atmosphere are adsorbed onto the TiO_2 surface. One of the most important constituents adsorbed onto the TiO_2 surface is H_2O which is

responsible for the generation of hydroxyl radicals. The $OH^{\cdot}$ which are created on the surface by the decomposition of absorbed H_2O are used directly in the oxidation process. Absorbed O_2 also plays a role as an electron/hole pair generator. Experimentally the O_2 which is adsorbed is equally important to the H_2O adsorbed; this will be further discussed in the results. Reactions between gas phase and adsorbed molecules use the Eley-Rideal model; reactions which involve two adsorbed molecules onto the semiconductor surface use the Langmuir-Hinshelwood model. This testing series is thus modeled by the Langmuir-Hinshelwood model and slight modifications to such. With reference to the experimental setup section the following reactions are used to describe the photooxidation of NO_x on the TiO_2 surface. First, all of the gases in the surrounding atmosphere are adsorbed onto the semiconductor surface; H_2O, O_2 and NO are the gases to be considered in equations (**54-56**).

$$TiO_2 + H_2O \leftrightarrow TiO_2\text{-}H_2O,\ k_{H2O} \quad \textbf{(54)}$$

$$TiO_2 + O_2 \leftrightarrow TiO_2\text{-}O_2,\ k_{O2} \quad \textbf{(55)}$$

$$TiO_2 + NO \leftrightarrow TiO_2\text{-}NO,\ k_{NO} \quad \textbf{(56)}$$

Since the H_2O is now adsorbed onto the TiO_2 as TiO_2-H_2O the production of hydroxyl radicals can occur. The adsorbed NO will remain until it reacts with a hydroxyl radical to form nitrous acid and the oxygen will become negatively charged from generated electrons. Next the quantum yield or electric potential will induce what we call electron/hole pairs and hole/electrons pairs which can be seen in equations (**57-59**).

$$TiO_2 + h\nu \rightarrow e^- + h^+, \phi \quad \textbf{(57)}$$

$$h^+ + TiO_2\text{-}H_2O \rightarrow OH\cdot + H^+, k_{h+} \quad \textbf{(58)}$$

$$e^- + TiO_2\text{-}O_2 \rightarrow O_2^-, k_{e-} \quad \textbf{(59)}$$

Thus, with the generation of the hydroxyl radical the chain reaction of oxidation processes can take place. We essentially have a reaction which follows: $NO \rightarrow HNO_2 \rightarrow NO_2 \rightarrow NO_3$ which can be seen in equations (**60-62**).

$$TiO_2\text{-}NO + OH\cdot \rightarrow TiO_2\text{-}HNO_2, k_{NO} \quad \textbf{(60)}$$

$$TiO_2\text{-}HNO_2 + OH\cdot \rightarrow TiO_2\text{-}NO_2 + H_2O, k_{HNO2} \quad \textbf{(61)}$$

$$TiO_2\text{-}NO_2 + OH\cdot \rightarrow NO_3^- + H^+, k_{NO2} \quad \textbf{(62)}$$

Here we can see the usually favored product of NO_3^-. Equation (**62**) shows the production of NO_2 on the surface of the semiconductor and its role in the production of NO_3^-. As has been shown in other studies, including this study, not all the NO_2 produced on the surface will be further catalyzed thus an increase in NO_2 concentration is to be expected. The thermodynamic recombination of electron/hole pairs or degradation of the electric field can be described by equation (**63**).

$$e^- + h^+ \rightarrow \text{heat}, k_{dea} \quad \textbf{(63)}$$

The recombination of unlike charges within the semiconductor gives off heat. This equation above will act as a drain for so called electron/hole pairs and will decrease the NO_x oxidation percentages. This problem generally results in an equilibrium in NO_x

concentration but can be an issue if the RH is low. Now the rest of the model is dependent of the equilibrium of the adsorption and desorption rates as seen in equation (**64**).

$$r_+ + r_- \rightarrow k_+ C_{TiO2\_free} C_{GAS} - k_- C_{TiO2\_GAS} = 0 \quad \textbf{(64)}$$

Thus, we have:

$$C_{TiO2\_GAS} = K_{GAS} C_{TiO2\_free} C_{GAS} \quad \textbf{(65)}$$

where GAS is NO, NO_2 or H_2O and $K_{GAS} = k_+/k_-$. After solving for C_{TiO2_free} the adsorbed gas concentrations can be solved for as seen in equations (**66-68**).

$$C_{TiO2\_NO} = \frac{K_{NO} C_{TiO2} C_{NO}}{1 + K_{NO} C_{NO} + K_{NO2} C_{NO2} + K_{H2O} C_{H2O}} \quad \textbf{(66)}$$

$$C_{TiO2\_NO2} = \frac{K_{NO2} C_{TiO2} C_{NO2}}{1 + K_{NO} C_{NO} + K_{NO2} C_{NO2} + K_{H2O} C_{H2O}} \quad \textbf{(67)}$$

$$C_{TiO2\_H2O} = \frac{K_{H2O} C_{TiO2} C_{H2O}}{1 + K_{NO} C_{NO} + K_{NO2} C_{NO2} + K_{H2O} C_{H2O}} \quad \textbf{(68)}$$

All the above concentrations occur at adsorption equilibrium. With these the following reaction rate models the NO_x adsorbed onto the semiconductor can be solved for

$$r_{NO} = \frac{-k_{NO} C_{TiO_2\_NO} \gamma C_{TiO_2\_H_2O}}{4k_{NO} C_{TiO_2\_NO} + 2k_{NO_2} C_{TiO_2\_NO_2}} \left(\sqrt{1 + \frac{4\alpha E_{rad}}{\gamma C_{TiO_2\_H_2O}}} - 1 \right) \quad \textbf{(69)}$$

$$r_{NO_2} = \frac{(k_{NO} C_{TiO_2\_NO} - k_{NO_2} C_{TiO_2\_NO_2}) \gamma C_{TiO_2\_H_2O}}{4k_{NO} C_{TiO_2\_NO} + 2k_{NO_2} C_{TiO_2\_NO_2}} \left(\sqrt{1 + \frac{4\alpha E_{rad}}{\gamma C_{TiO_2\_H_2O}}} - 1 \right) \quad \textbf{(70)}$$

and the ratio of the dot product of electron and hole pair reaction rate constants over the reaction rate constant for recombination:

$$\gamma = \frac{k_{h^+} \times k_{e^-}^*}{k_{dea}} \quad \textbf{(71)}$$

where $k_{e^-}^* = k_{e^-} C_{TiO_2'-O_2} = k_{e^-}((K_{O_2} C_{TiO_2'} C_{O_2})/(1 + K_{O_2} C_{TiO_2'} C_{O_2}))$.

Additional NO_x Chemistry[19]

Prior literature and this project have shown the photoelectrochemical oxidation of NO_x with TiO_2 generates NO_2. As the input NO concentration increases the output NO_2 produced in the electrochemical process also increases. This produced NO_2 reaches an equilibrium state as the rate of produced NO_2 equals the rate of oxidized NO_2. The desired product in this process is NO_3^-, however there are two products which must come first before NO_3^- is produced. These products are HNO_2 and NO_2. Also, there are several chemical reactions involving nitrogen oxides which may impact the overall NO_x chemistry. These reactions are:

$$NO_2 + h\nu \rightarrow NO + O \quad \textbf{(72)}$$

$$NO_3 + h\nu \rightarrow NO + O_2 \quad \textbf{(73)}$$

$$NO_3 + h\nu \rightarrow NO_2 + O \quad \textbf{(74)}$$

$$HNO_2 + h\nu \rightarrow NO + OH \quad \textbf{(75)}$$

$$O + NO_2 \rightarrow NO + O_2 \quad \textbf{(76)}$$

$$O + NO_2 \rightarrow NO_3 \quad \textbf{(77)}$$

$$NO + NO_3 \rightarrow 2NO_2 \quad \textbf{(78)}$$

$$O + NO \rightarrow NO_2 \quad \textbf{(79)}$$

$$NO_2 + NO_3 \rightarrow N_2O_5 \quad \textbf{(80)}$$

$$N_2O_5 \rightarrow NO_2 + NO_3 \quad \textbf{(81)}$$

$$HO_2^{\cdot} + NO \rightarrow NO_2 + OH^{\cdot} \quad \textbf{(82)}$$

$$OH^{\cdot} + NO_2 \rightarrow HNO_3 \quad \textbf{(83)}$$

and as seen above there are many products which can occur. The desired chemical path for NO using the photoelectrochemistry of TiO_2 was described prior, but nature does not always do what we want. Chemical paths which deviate from the established chemical paths in equations (**72-83**) are more likely to occur in Earth atmosphere as opposed to a sealed chamber in a lab. The results section shows very consistent NO_x oxidation thus a number of these reactions above are not occurring in the chamber. If these reactions are occurring, then the product concentration is not high enough to impact the test. For instance, if equation (**72**) occurs for all NO_2 in the chamber then NO_3^- would never be created and the input NO would be stuck in an infinite loop. Obviously, this does not occur due to the NO concentration decreasing after the quantum source or LED is turned on.